Failure of Laminated Composites at Thickness Discontinuities Under Complex Loading and Elevated Temperatures

Thesis by

Sangwook Lee

In Partial Fulfillment of the Requirements
for the Degree of
Doctor of Philosophy

California Institute of Technology
Pasadena, California

1998
(Submitted March 30, 1998)

Acknowledgements

This work was supported by NASA Langley Research Center under NASA Grant NSG 1483 with Dr. J. H. Starnes as the monitor. The financial support of Korean government through scholarship is appreciated.

I would like to acknowledge my advisor Professor Wolfgang G. Knauss for his ideas, guidance, and support throughout my study at GALCIT. He also showed me the importance of physical insight during the two years I worked as a teaching assistant of Ae102 class. I am grateful to all the other professors in solid mechanics group; Prof. Rosakis for his clear presentation in many classes, Prof. Ravichandran not only for the use of his laboratory equipment but also for the many discussions on non-technical subjects, and Prof. Ortiz for his inspiring class on computational mechanics. I also would like to thank the other member of my thesis committee, Prof. O. Bruno of applied mathematics, for taking the time to review the dissertation.

Many people helped me in conducting experiments. I am grateful to Dr. Hongbing Lu, now at the Oklahoma State Univ., for introducing me experimental techniques. The acoustic emission setup by Dr. Mark Walter, now at Ohio State Univ., played important role in my work. A debt is owed to many artisans for their advice and help, especially Joe Haggerty, Larry Frazier, and Ali Kiani in aeronautics machine shop. Jonh van Deusen and Rodney Rojas in students machine shop were also essential to the fabrication of loading frames. I am indebted to Mr. Allen Waters of NASA/Langley for providing the specimens including cutting and C-scanning.

I am particularly fortunate to have had Dr. Allan Zhong, now at Goodyear research center, to teach me how to do finite element analysis with ABAQUS and to use Cray 90. His help and suggestion regarding numerical work is gratefully acknowledged. The finite element computations were conducted on the Cray 90 at the NSF

supported Supercomputing Center of the University of California at San Diego.

My life was enhanced by many friends at GALCIT, especially dwellers of our big office; Samudrala Omprakash, Pradeep Guduru, Demir Coker, Bibhuti Patel, and Javier Gonzalez. Dicussions with Han Park, the only other Korean speaker at GALCIT, were certainly very enjoyable part of living at Caltech. He kept me informed of the other half of GALCIT, fluid mechanics.

Finally, I would like to give my special thanks to my wife, Sanghee. Her *support, patience,* and *sacrifice* made it possible for me to concentrate on my work at office and laboratory. The acknowledgement can not be completed without mentioning my lovely son, Dohyeong, who has started his life with my study at Caltech.

Abstract

Failure initiation of laminated composites with discontinuous thickness is examined in terms of typical structural load description (tension, shear force and bending moment) rather than in terms of micromechanics considerations. Because transverse shear produced relatively small effects in failure initiation, results are presented as tension-bending interactions. Two loading frames were designed to apply moments and tension simultaneously. Four types of specimens of different stacking sequence were examined to determine failure initiation, and analyzed subsequently via a finite element analysis (ABAQUS). Depending on the stacking sequence across the interface of the step, two different failure modes are identified: For uni-directional fiber orientation across the interface in the tension direction, failure occurs through cracking and delamination which is governed by a fracture mechanics criterion. While the initiation strength for this failure mode is higher than for the cross-ply configurations, the residual strength after initiation is only marginally higher, providing virtually no margin of safety (10%). For cases involving cross-plies on either side of the interface, failure initiation occurs by matrix cracking, with a critical strain across the fibers providing a universal failure criterion. In these cases the residual load bearing capability was 30 to 45% higher than the failure initiation loads. The interaction between moment and tension at failure initiation is linear, an observation that does not hold for the delamination failure driven by crack propagation. It is found that all failures can be described in terms of a common fracture principle; the stress or strain criteria are interchangeable with the fracture energy computations, provided one allows for a range of values of associated fracture energies. Assuming that time dependent aspects of the failure process are not dominant, elevated temperatures did not change the general results of how bending and tension loads interact, provided one accounts for residual thermal stresses; however, the stress magnitude at which the failure initiation occurs decreases with increasing temperature.

Contents

List of Figures

List of Tables

Chapter 1 Introduction

The technology of composite materials has experienced a rapid development in the last two decades. One primary motivation for this development is the requirement for high performance materials in aircraft and aerospace structures [1]. Advanced composites have superior mechanical properties, including high stiffness-to-weight ratio, high strength-to-weight ratio, excellent fatigue resistance, corrosion resistance, low thermal conductivity, and the ability to be tailored to a particular need. The most recent and challenging uses of composites are perhaps the FY-22 and B-2 [2]. The former contains more than 50% composites, and the latter mostly composites. The B-2 stealth bomber uses graphite/epoxy and high temperature polymeric composites. The Boeing 757 commercial aircraft has also a large number of composite material components. The widespread use of composite materials reflects that notable advances have been made in understanding the special design considerations that set composites apart from the usual isotropic engineering materials such as metals.

However, the innovative structural concepts and use of advanced materials are necessary for future aircrafts to satisfy stringent requirments. A Mach-2.4 supersonic aircraft, HSCT (High-Speed Civil Transport), drives the materials and structures development [3]. The fraction of the operating empty weight for airframe structure is much smaller for a supersonic transport than for conventional subsonic commercial vehicles. The operating environment is also more severe because of the high temperatures associated with the aerodynamic friction heating caused by supersonic cruise speeds. To lighten the fuselage, outboard wing, and empennage, carbon fiber-polymer matrix must be used.

A recurring problem in designing structures with fiber reinforced composite materials is the potential failure at thickness variations in the lay-up which results from associated stress concentrations. Such questions arise in connection with stress vari-

ations in the vicinity of geometric discontinuities in the ply drop-off problem as well as with attachments of stringers and other frame structures to the skin of aircraft, for example (See Figure 1.1). With respect to the solution of structural instabilities, the post buckling strength is of considerable importance for the fail safe evaluation of current designs. Thus, a knowledge of when and how the degradation and loss of such shell stiffening impacts global structural strength is mandatory for design purposes. However, in spite of the importance of stress concentrations to failure initiation, many issues related to this topic for laminated composites are still in the early stages of development [2].

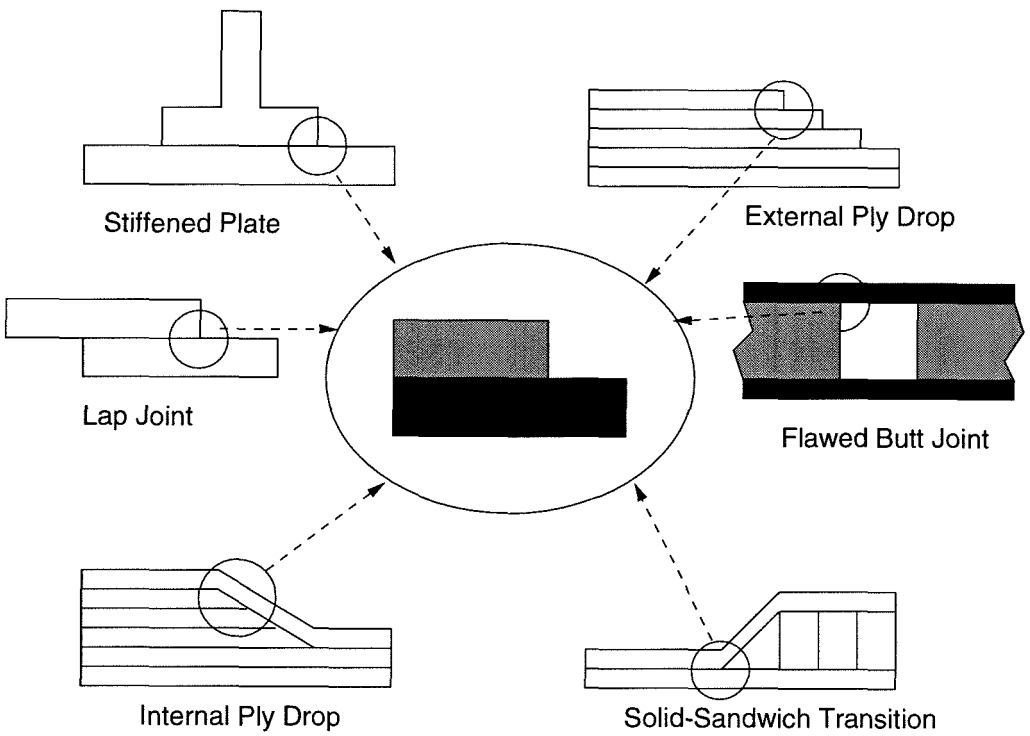

Figure 1.1: Examples of sharp corner in composite structures

1.1 Previous Research

Within the framework of solid mechanics, any failure emanating from "sharp" corners elicits immediately the vision of stress singularities and analyses associated with the discipline of fracture mechanics. Previous examinations of this and related problems have been addressed by others, primarily through analytical/computational means. Based on generalizations of linearly elastic fracture mechanics, these studies assume that the onset of fracture is predicted in terms of a fracture toughness parameter. Lin and Hartman [4] obtained stress singularities for bonded anisotropic wedges under generalized plane strain conditions in terms of Lekhnitskii's complex variable method (complex eigenvalue problem). Zenkert et al. [5] applied this result to suggest a failure criterion for fracture initiation at sharp 90^o corners in an imperfect butt joint by assuming that onset of fracture may be predicted in terms of a (corner) stress intensity factor and a fracture toughness parameter. Kassapoglou and DiNicola [6] suggested an efficient stress estimate at skin-stiffener interfaces to reduce the cost of theoretical and finite element analyses, the results being intended for use by structural designers at the early stages when trade-off studies are performed. For the same purpose Bhat and Lagace [7] presented an estimation method for a quick evaluation of interlaminar stresses at material discontinuities. Experimental studies on the effect of ply-drop configuration on delamination strength have been carried out by Botting et al. [8] with an attendant (three-dimensional) finite element to determine maximum shear and von Mises stresses as a measure of delamination initiation. In a similar vein Hyer et al. [9] determined stresses experimentally around a stiffener/skin interface in pressure-loaded composite panels to reveal the three-dimensional nature of stresses around sharp corners. These studies essentially focused all on the effects of very localized (small size scale) singularities or stress concentrations.

As part of the motivation for the work reported here, Kubr [10] performed an analytical/numerical study of the stress field surrounding a step discontinuity in a composite in order to lay the groundwork for further experimental examinations. Treating each ply as a continuum with anisotropic properties and the corner as a

mathematically sharp 90^o feature as the origin of a (polar) coordinate system, it was found that the stresses were of the form $\sigma_{ij} = \Psi_{ij} r^k$ and thus similar to the Williams solution for a wedge in an isotropic material [19]. Employing a highly refined finite element mesh, plots of $\log(\sigma) - \log(r)$ were used for each stress component to determine k and Ψ by fitting a straight line to the log-log plots, the procedure followed also by Zenkert et al. [5]. However, it turned out that the power law stress singularity field applied only within a region of less than $10^{-1} \mu m$ from the base of the corner, the solution deviating markedly from the assumed power law outside of that domain. Considering that the fiber diameter is about 7 μm, the singularity field exists thus in such an extremely small region that continuum concepts for "smeared-out" ply properties are not applicable at that size scale.

In an experimental follow-on study, Gortsema [11] showed with the aid of optical microscopy that in a realistic situation, *i.e.*, in the absence of a "mathematically sharp corner,"[1] the location of a stress singularity was not the immediate site of failure initiation. At the size level of the ply-thickness, the corner was not "analytically" sharp, regardless of how carefully the specimen preparation was carried out. Failure originated consistently at points away from the interior corner of the step-down; this distance from the "corner" was measured typically in terms of one or a few ply-thicknesses.

1.2 Objective of This Work

The Kubr-Gortsema studies thus demonstrated clearly that micromechanical considerations cannot then dominate structural failure analysis and that macroscopic failure proclivity must be evaluated at an appropriate size scale. Moreover, from a design point of view it is desirable to evaluate structures in terms of "strength of materials" loads such as moments, (average) shear and tension stresses (See Figure 1.2). At issue is thus whether a failure criterion can be established that lends itself to structural

[1] Microscopic examination of "corners" reveals quickly that even in carefully prepared specimens, typically a (rough) fillet exists, the radius of which is on the order of a ply-thickness.

applications. Even if the basis of such a criterion rests in the mechanics at the micron or submicron scale, it may be possible to employ minimum test data to establish a "macroscopic" criterion or criteria which can be evaluated with the aid of a minimal number of relatively simple laboratory tests.

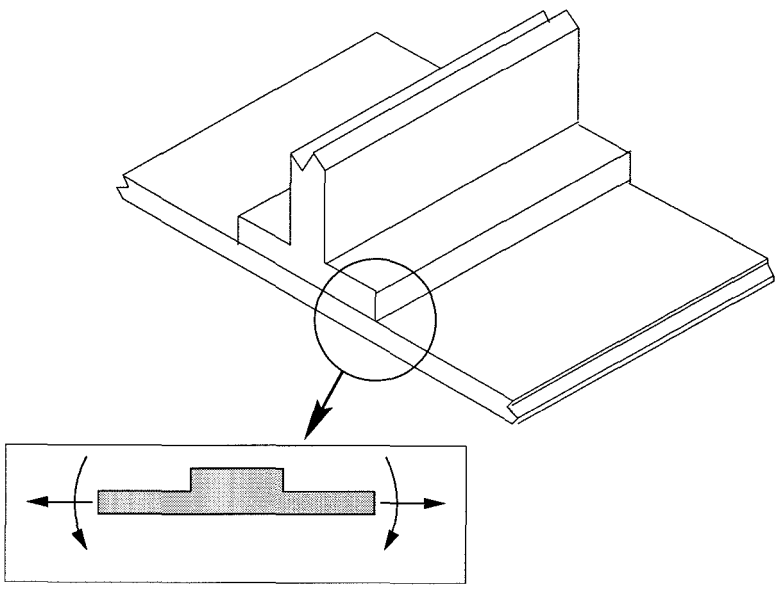

Figure 1.2: Loads on step-down section

In the past, experimental studies have been conducted at environmental (room) temperatures. However, with the prospect of high speed air-transports and associated elevated temperatures in both primary load carrying as well as engine-close structures, the possible degradation of structural performance due to raised temperatures must be considered. This is especially true for polymer matrix materials which become very temperature sensitive as their glass transition temperature is approached. It is thus important to evaluate in which temperature range below the glass transition structural penalties become unacceptable. This temperature sensitivity manifests itself primarily in terms of increased time dependent (creep) behavior, which, even at temperatures well below the glass transition ($20-30^{o}C$), may give rise to accumulated effects if repeated thermal cycles are involved. Although we recognize the importance

of the time dependent behavior in the failure process of composite materials, we prefer to take here a somewhat simpler point of view and consider temperature merely as a parameter which affects the failure strength of the composite potentially without a major complication in the form of time dependent (creep) response of the matrix. However, it is then still of interest to ask whether the failure mode(s) or mechanism(s) of failure initiation (and progression) are changed by elevating the temperature.

It appears self-evident that the ply sequence across the "interface" between the step-up and the base plays a significant role in the failure initiation process. For definition purposes we refer to the step-up as the "stiffener" (thicker portion) in Figure 2.1, while the thinner portion is called the plate, the two portions being separated by the "interface." From a physical point of view, the "interface" is formed by co-curing the specimens and as such does not represent a manufacturing interface in the sense of an adhesive bond. The term is used here only for spatial identification purposes. Because the layers adjacent to this interface can control the failure behavior, it was appropriate to include in this study several lay-ups that are likely to be representative of a large range of possible lay-up configurations, a number of four being deemed sufficiently indicative.

The tenor of this study is primarily experimental in nature, with, however, a strong component of numerical analysis in order to better understand the micromechanical basis for the observed failure behavior. In the next chapter, the specimen lay-up and the experimental arrangements are presented including identification methods of failure initiation at room and elevated temperatures. The failure behavior, which exposes two operative failure criteria depending on the type of lay-up across the interface, is described in chapter 3. In chapter 4 the analysis based on the commercial finite element code ABAQUS is presented. Although the emphasis here is on failure initiation, we also track the residual strength of the specimens once failure initiation has occurred to final destruction. This exposition is followed in chapter 5 by results at elevated temperatures. We conclude with a summary of the failure behavior.

Chapter 2 Experimental Set-Up

The experimental work comprises three major components, namely the design and manufacture of the specimens, the means of providing the combined loading and the method of observing failure initiation. These items are considered sequentially next.

2.1 Specimens

The geometry of a typical specimen used in this study is shown in Figure 2.1. The length of the specimen is 30.5cm (12in) and the width is 2.5cm (1in). Because structures contain, in general, multidirectional plies, a finite width specimen develops, per force, three-dimensional deformations in the vicinity of the corner, and, in fact, all along the edges of the specimen [15]. There was no simple, economical way to obviate this disadvantage in favor of a more two-dimensional configuration; this fact has both experimental as well as analytical consequences that need to be addressed without approximation. The consequence of this needs to be reflected in the (finite element) analysis later on.

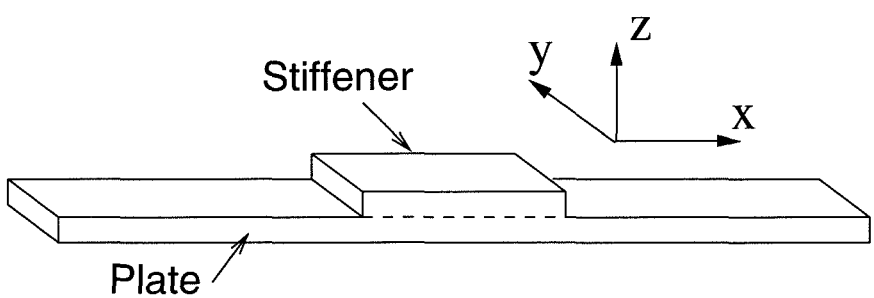

Figure 2.1: Specimen configuration

The specimens were manufactured of AS4/3502 carbon fiber reinforced epoxy at the NASA Langley Research Center. The thicker portion of the specimen (stiffener) was co-cured with the base plate. The specimens were fabricated as a single, stepped

Type	Plate	Stiffener
I	$[90,45,0,-45]_s$	$[0,-45,90,45]_s$
II	$[90,-45,0,45]_s$	$[90,45,0,-45]_s$
III	$[-45,90,45,0]_s$	$[45,90,-45,0]_s$
IV	$[0,-45,90,45]_s$	$[0,45,90,-45]_s$

Table 2.1: Stacking orders of the specimens

plate, which was then cut with a diamond blade into individual specimen strips after the curing/cooling cycle was completed. After the specimens were cut, each one was C-scanned to ensure that neither delaminations nor inclusions could be observed[1]. The cut edges of the specimens were polished with a 3000 ($6\mu m$) grit diamond paste in order to reveal the fiber structure and to allow succinct observations of failure initiation.

Four types of specimens with different stacking order were studied. The four lay-ups, each one identified as a "Type" with a Roman numeral, are described in Table 2.1. The fiber direction of 0^o is parallel to the x-axis and positive fiber angles are measured from this axis in the counter-clockwise direction with the thick portion towards the viewer. The orientation of each ply is listed in the order it is layed up, from bottom to top in Figure 2.1, and the subscript S refers to a symmetric lay-up. As an example, the plate lay-up for Type I $[90,45,0,-45]_S$ is written explicitly as [90, 45, 0, -45, -45, 0, 45, 90]. The thickness of a ply is 0.25mm (0.01in).

Because of the lay-up a coupling exists between bending and twisting ($D_{16} \neq 0$), although most coupling terms vanish ($B_{ij} = 0$ for $i,j = 1,2,6$ and $A_{16} = A_{26} = 0$). The meaning of the coupling terms are given below. In the experiments the twist mode was restrained in order to represent, in part, wide panels in structures as far as possible; however, the analytical model accounts for this effect.

[1]The author is indebted to Dr. J. H. Starnes and Mr. Allen Waters of NASA/Langley for providing the samples, including cutting and C-scanning.

The laminate constitutive relations

The force-deformation (reference plane strains) and moment-deformation (reference curvatures) relations of multidirectional laminates are given by the following expression.

$$\left[\begin{array}{c} N_1 \\ N_2 \\ N_6 \\ \hline M_1 \\ M_2 \\ M_6 \end{array}\right] = \left\{\begin{array}{ccc|ccc} A_{11} & A_{12} & A_{16} & B_{11} & B_{12} & B_{16} \\ A_{12} & A_{22} & A_{26} & B_{12} & B_{22} & B_{26} \\ A_{16} & A_{26} & A_{66} & B_{16} & B_{26} & B_{66} \\ \hline B_{11} & B_{12} & B_{16} & D_{11} & D_{12} & D_{16} \\ B_{12} & B_{22} & B_{26} & D_{12} & D_{22} & D_{26} \\ B_{16} & B_{26} & B_{66} & D_{16} & D_{26} & D_{66} \end{array}\right\} \left[\begin{array}{c} \epsilon_1^o \\ \epsilon_2^o \\ \gamma_6^o \\ \hline \kappa_1 \\ \kappa_2 \\ \kappa_6 \end{array}\right] \tag{2.1}$$

where

$$A_{ij} = \sum_{k=1}^{n} Q_{ij}^k (h_k - h_{k-1}), \quad B_{ij} = \frac{1}{2} \sum_{k=1}^{n} Q_{ij}^k (h_k^2 - h_{k-1}^2), D_{ij} = \frac{1}{3} \sum_{k=1}^{n} Q_{ij}^k (h_k^3 - h_{k-1}^3)$$

with $i, j = 1, 2, 6$.

N_i and M_i are stress and moment resultants, respectively. The matrices A_{ij}, B_{ij}, and D_{ij} for the four types of specimen are given in Appendix.

2.2 Loading Devices

In order to apply combined loading to the specimens, two devices were designed as described below. However, before these details are considered, it should be pointed out that tests involving three and four point bending involve different degrees of transverse shear. Because no significant differences were observed in performing three- and four-point bending as will be shown in chapter 3, it was concluded that transverse shear played a secondary role in the failure behavior, and in the sequel only tension-bending interactions will thus be discussed.

2.2.1 Simple Tension

Contrary to a test of uniformly cross-sectioned specimens, simple tension applied to the ends of a specimen produces bending. The deflection and moment distribution can be estimated from beam theory. The deflection and moment distribution (with respect to the midplane) under a tension of T = 3736N (840lbs) are shown in Figure 2.2. Since the reference plane is different for the plate and thicker portion, a jump occurs in the moment distribution at the step-down section (x = 11.4cm (4.5in)). The results from beam analysis are compared in that figure with those from the finite element analysis (ABAQUS).

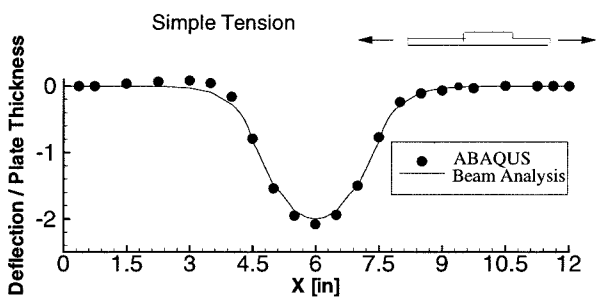

(a) Deflection

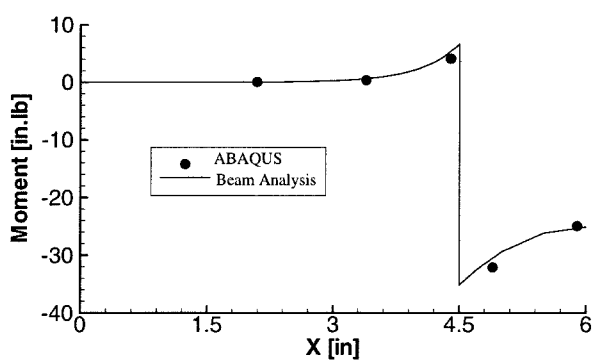

(b) Moment Distribution

Figure 2.2: Deflection and moment of Type I - Simple tension T=840 [lbs]

Determination of deflection and moment from beam theory

A simple theory of beams of composite materials is developed in [13]. It was assumed that the deflection was uniform across the specimen; *i.e.*, all the variables are independent of y coordinate. Because $B_{ij} = 0$ for $i, j = 1, 2, 6$ and $\partial/\partial y = 0$, the moment-curvatures relations in equation (2.1) are simplified for a beam to

$$M_x = D_{11}\kappa_x = D_{11}\frac{d^2w}{dx^2} \tag{2.2}$$

where w is the deflection in the z direction.

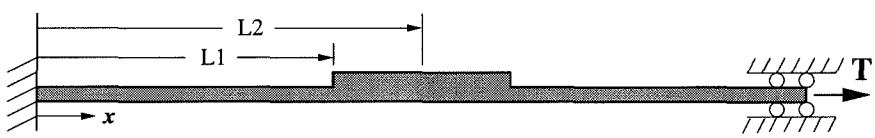

Figure 2.3: Simple tension of fixed-end specimen

The governing equations for the specimen under tension T in Figure 2.3 are

$$M(x) = D_{11}^p\frac{d^2w}{dx^2} = Tw(x) - M_R \quad (0 \le x < L_1) \tag{2.3}$$

$$M(x) = D_{11}^t\frac{d^2w}{dx^2} = T[w(x) - w(L_1)] + Td + M(L_1) \quad (L_1 \le x \le L_2) \tag{2.4}$$

D_{11}^p and D_{11}^t are bending stiffness parameters of the plate and thick portion ($L_1 \le x \le L_2$), respectively. M_R is the reaction moment at $x = 0$. d is the distance between the reference planes for the plate and thick portion, which is 1.02mm (0.04in) for these specimens.

At $x = 0$ the deflection needs to satisfy the boundary conditions; $w = 0, dw/dx = 0$. Because the deflection is assumed to be symmetric with respect to $x = L_2$, the slope at $x = L_2$ is zero. The two deflections from equation (2.3) and (2.4) are required to match smoothly at $x = L_1$.

The solution of the governing equations with the boundary and continuity conditions determine the deflection and moment distribution, which are shown in Figure 2.2

for tension T=840[lbs].

2.2.2 Loading Device I (non-proportional loading)

The straining device shown in Figure 2.4 was used for tests involving three- and four-point bending. It was designed to draw on the tension/torsion capability of the MTS system. The tension is provided by the test machine in the standard fashion, but the torsional mode was translated through an appropriate linkage system into a lateral force F for providing the lateral deflection so as to impose bending and tension loads in arbitrary sequence (non-proportional loading). The accompanying lateral force was recorded by a compression load cell.

This loading device allows independent histories of deformation in the two (three) loading modes. Loading with this appliance was conducted typically by straining the specimen to a desired tensile load and keeping that load constant under load control mode. Then the lateral force was applied to bend the specimen.

2.2.3 Loading Device II (proportional loading)

A second loading frame, also used for combined tension/bending tests but under a proportional loading scenario, is shown in Figure 2.5. The specimen is located off the tension axis. As the specimen is pulled, both tension and moment on the step-down section increase simultaneously and roughly proportionately as shown in the loading path in Figure 2.5. The moment is changed by adjusting the eccentricity e. Simple tension results with this frame for some fixed value of e. As explained above, a positive bending moment exists if only a tensile load is applied. However, if e takes on some negative value, pure tension, *i.e.*, a condition of nearly zero moment, can be achieved. The range of e was from -0.1in. to 0.5in. The operation of this appliance was much simpler than the other one, and was used primarily. This is referred in the sequel as the "proportional loading frame." Because the results derived from either loading device did not differ within the range of data scatter, the loading path was judged unimportant in this study.

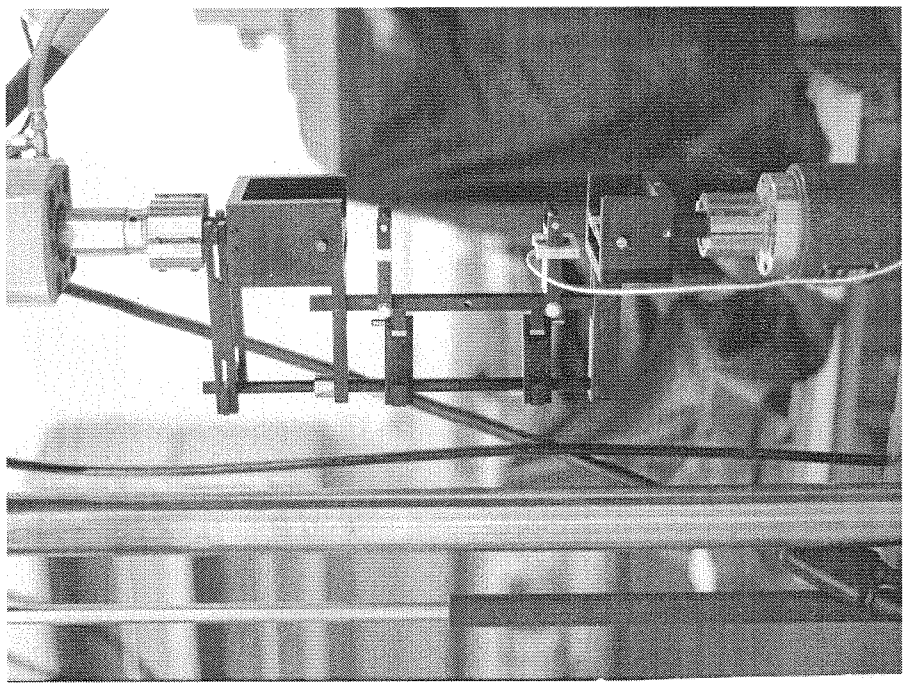

(a)

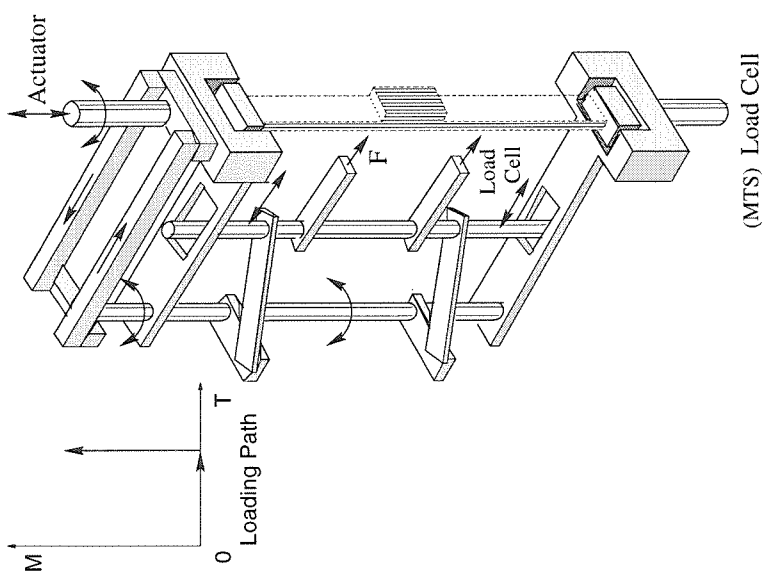

(b)

Figure 2.4: Loading frame for three- and four-point bending coupled with tension

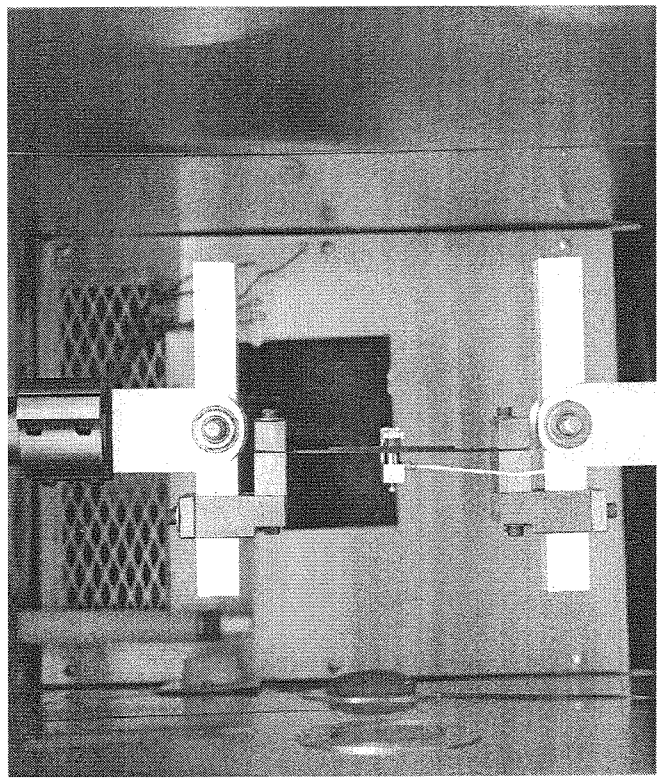

(a)

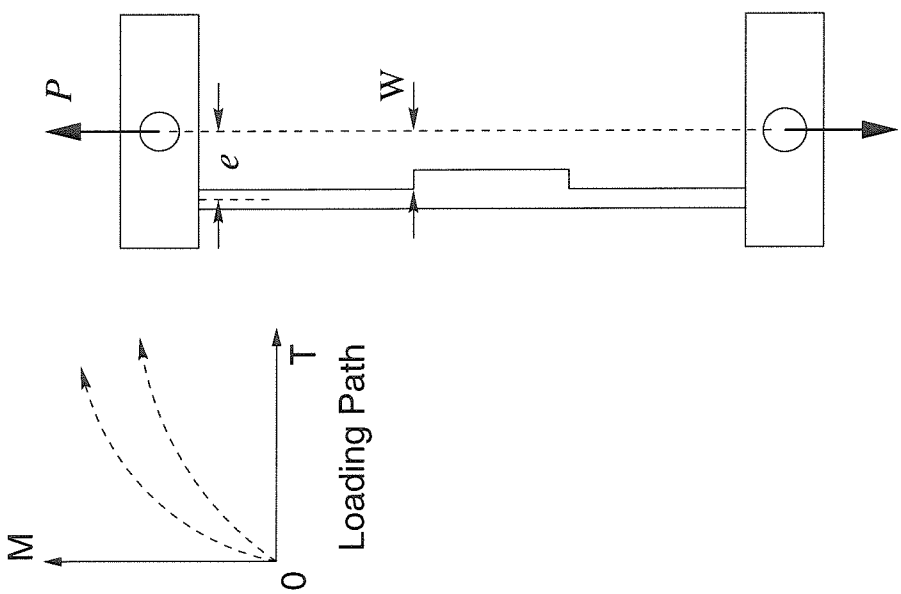

(b)

Figure 2.5: Loading frame for proportional moment/tension loads

A device for measuring the deflection w

Because the deformations were classified as "large," being on the order of or larger than the specimen thickness, the bending moment needed to take the deformations into account. The bending moment M was determined by measuring the distance, w, between the line of tension and the mid plane of the step section in the deformed configuration as $M = Pw$ for a tensile load P. From this relation, it can be readily appreciated that a small error in e induces a corresponding moment error. It was thus imperative to measure w precisely.

Accordingly, the traversing device carrying a low power microscope (magnification 4x) in Figure 2.6 was used. The resolution of the device was 0.025mm (0.001in). This method was also selected to measure w because its non-contact method of operation can also be used for measurements at elevated temperatures. Any type of contact measurement, for example a traveling indicator, can exert an undesirable lateral force on the specimen.

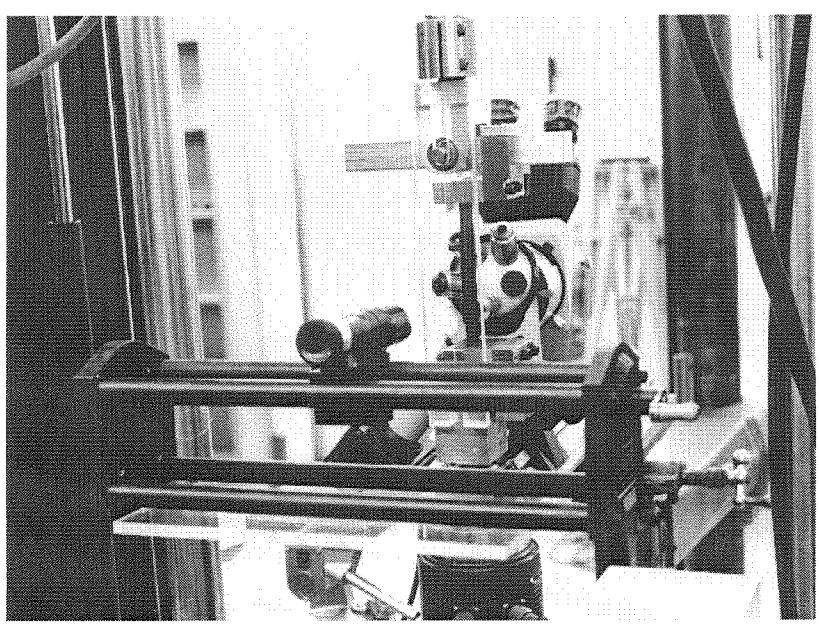

Figure 2.6: Device for measuring the moment arm

In combined load test with the proportional loading frame (Figure 2.5), specimens were cut short because the original (long) specimens often broke at an end of the specimens near a grip, rather than at the step section. The reason was that the central part of the specimen was deflected to the line of tension so that the bending moment was small at the specimen center, but not at the end of the specimen.

2.3 Failure Observations

At room temperature observations of failure initiation were made with the aid of a stereo microscope while the specimen was under load. The microscope was placed on a mount possessing three degrees of freedom which allowed following the region of interest undergoing deformation as first cracks appeared (see Figure 2.7).

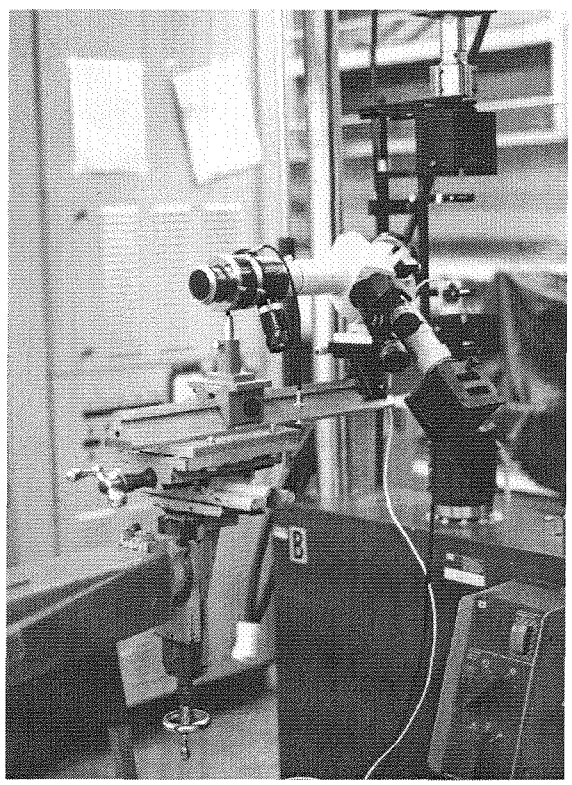

Figure 2.7: Microcsope mount

This feature provided the ability to track the corner of interest and its surroundings as its position and orientation changed during the loading process. According to the analysis, the region of highest stresses was well identified for Type I and II specimens so that the location of the failures was reasonably well identified at the edge of the specimens after a few trials. Attachment of an optical camera to the microscope and a polished surface finish on the specimen edge permitted thus the recording of the various features in the damage development during the test. Accompanying the optical record, ply cracking produced an audible energy release, a feature that became important in situations where cracking was difficult to observe on the specimen edge directly, as, for example, at elevated temperatures or with specimens of Type III. In the latter the top lamina of the plate had the fibers running at 45^{o} with respect to the tension axis and initial cracking did not always occur near the specimen edge but somewhere along the corner of the step. In these situations the crack-induced audio signal noted the failure. At this point the test was stopped and a dye-penetrant was used to verify that a crack had formed. For tests at elevated temperatures, the audible signal was used exclusively as a failure indication because microscope observation became virtually impossible through the multiple glass panes of the temperature control chamber.

Chapter 3 Failure Behavior

The failure behavior clearly depends on the stacking sequence, differentiated here primarily in terms of the ply orientation next to the interface. We delineate the major differences between these sequences and examine the commonality in their failure behavior based on well accepted criteria in the fiber composites community. The experimental results are discussed first in this chapter, followed by the analytical part in next chapter. A summary of the failure patterns associated with the four stacking sequences is sketched in Figure 3.1: Although not all laminae are shown for reasons of clarity of presentation, the ply orientation near the interface is properly identified.

3.1 Type I and Type II Specimens

The dominant and consistent failure mode of Type I and II specimens was by matrix cracking. In the top ply of the base which is next to the interface, the fiber direction is at an angle of 90^o with respect to the tension axis. The lamina across the interface has a fiber direction of 0^o. Because the plies are weakest in the direction normal to the fibers, the tension/bending induced stress component normal to fibers causes the ply to crack. Photographs of typical crack near a corner are shown in Figure 3.2. Some cracks occur at locations away from the corner as reported by Gortsema [11]. One reason for this behavior is the shape of corner which is "filleted" rather than sharp.

The failure response of specimens of Type I and II is governed by their lay-up similarity: For both types the stacking sequence of the plate are the same, though the stiffeners possess different ones, namely [0,-45,90,+45]s for Type I and [90,-45,0,+45]s for Type II, so that the stiffener lamina has either a 0^o or a 90^o orientation. The

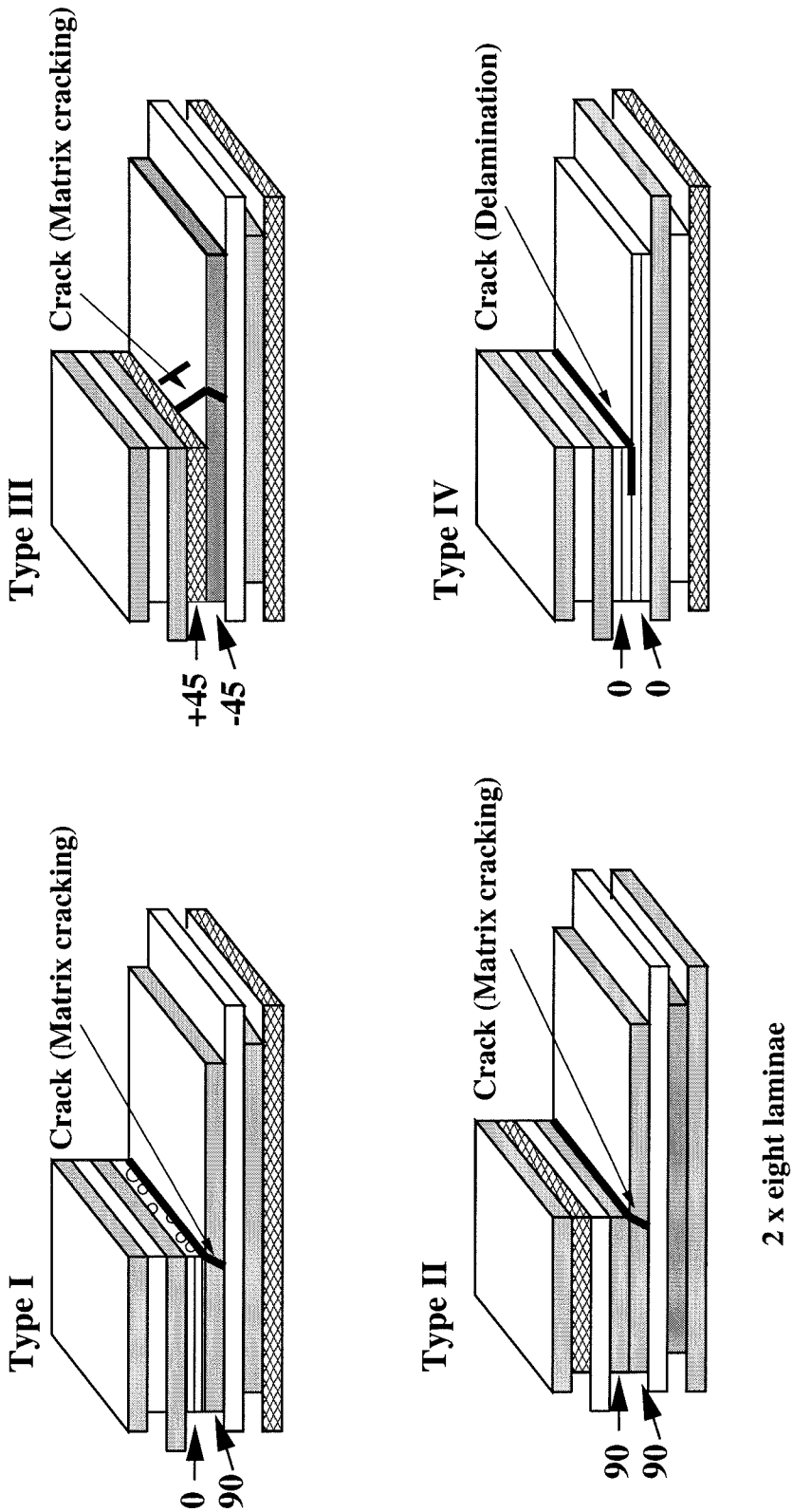

Figure 3.1: Failure modes

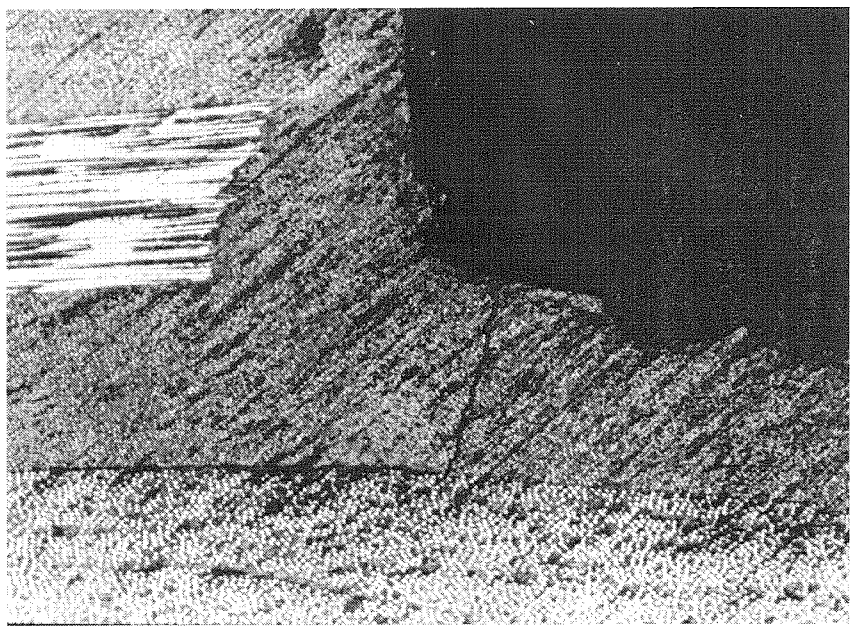

(a)

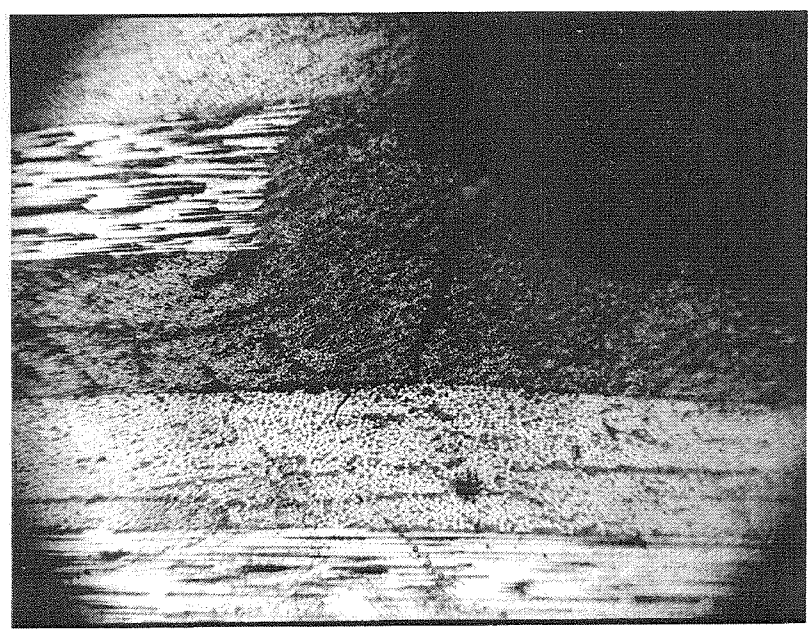

(b)

Figure 3.2: Matrix cracks in Type I & II specimens

Specimen	3-Point Bending [lb-in]	Pure Bending	Failure mode
Type 1	15.32	16.17	Matrix cracking
Type 2	N/A	19.34	Matrix cracking
Type 3	20.09	25.04	Matrix cracking
Type 4	44.01	43.67	Delamination

Table 3.1: Bending moments at failure initiation

interaction between moment and tension at failure initiation for the two lay-ups are presented in Figure 3.3 along with numerical results to be described in the next chapter. Disregarding the analytically developed lines for now, we note that in spite of the large deformations, the interaction between moment and tension at failure is roughly linear. Note also that the load levels for the Type II specimens are typically higher by about 25% than those for the Type I specimens.

The effect of the shear force on failure seemed to be negligible from the results of 3-point and 4-point bend tests. The bending moments at failure initiation from the two tests are nearly the same for all the four types of specimens as shown in Table 3.1.

While the emphasis in this work was on the initiation of failure as a conservative failure criterion for structural purposes, in some of the four-point bending tests, loads were increased after an initial crack appeared to check the residual load carrying capability. It was found that for the ply lay-ups studied here, this load at ultimate failure was about 30-45% higher than that at initiation. The magnitude of moment at crack propagation is compared with the moment at crack initiation in Table 3.2. For further details on the crack propagation to ultimate failure, the interested reader is encouraged to consult Gortsema [11]. Suffice it here to state that after the top ply had been broken in the initial fracture process, a matrix crack propagated along the interface of the first and second plies of the specimen (see Figure 3.4). This (intermediate) delamination process was rather slow and virtually no sound of the process was audible. However, the next and final phase of the failure process involved further complex delaminations accompanied by noisy matrix cracking in adjacent plies.

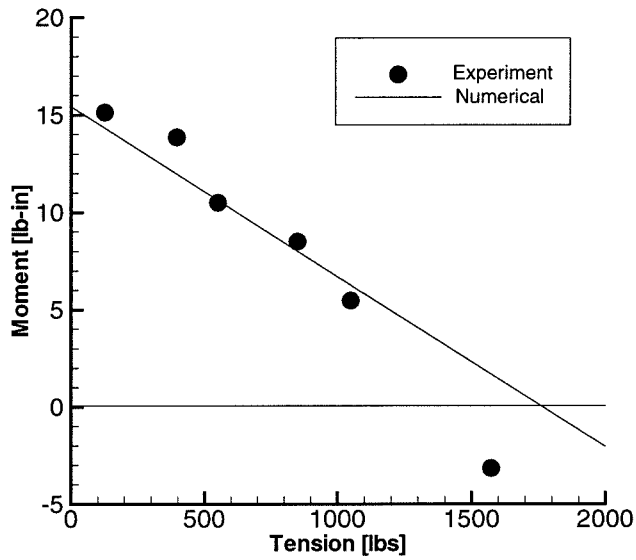

(a) Type I

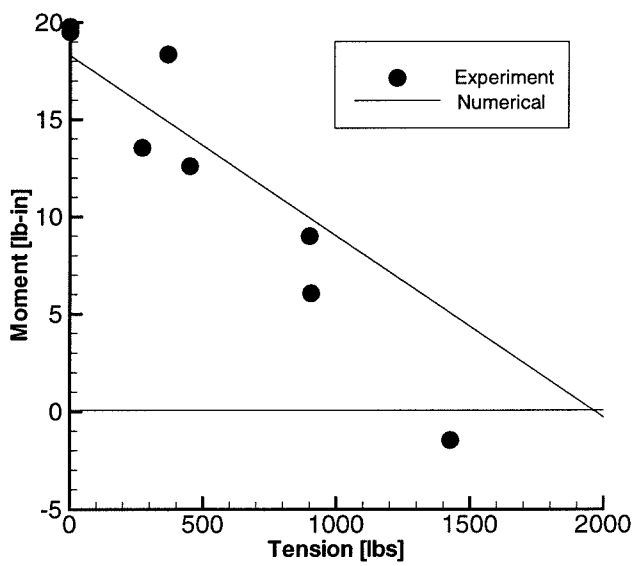

(b) Type II

Figure 3.3: Failure curves for Type I and II

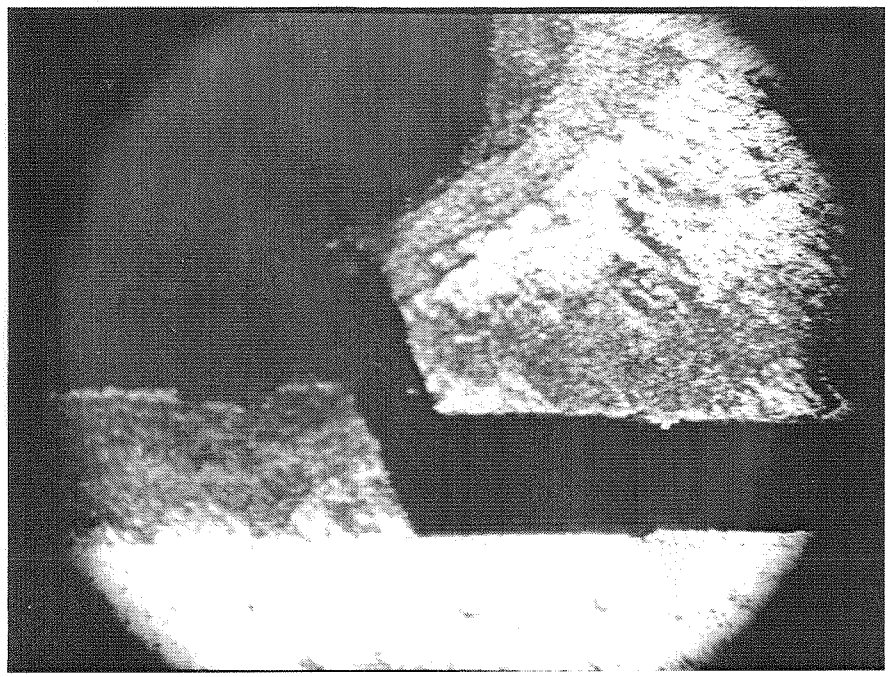

Figure 3.4: Crack propagation of Type I specimen

Specimen	Test	Initiation moment	Propagation moment	Difference
Type 1	4-point bend	19.34 [in.lb]	26.18 [in.lb]	35%
	4-point bend	16.17	23.52	45%
	3-point bend	15.32	20.09	31%

Table 3.2: Comparison of crack initiation and propagation moments - Type I

3.2 Type III Specimens

The layers across the interface in this specimen are oriented in the $\pm 45^o$ directions, resulting in crack formation in the top lamina of the plate and parallel to the fibers (tension across the fiber axes). Because the crack formation did not always start at the specimen edge, it was also not always possible to identify initial failure through microscope observation. In these cases the acoustic sound was used to identify failure onset: the test was stopped and the surface examined for cracks with the microscope and with a dye-penetrant[1]. A picture of the latter situation is reproduced in Figure 3.5, and the failure interaction plot is given in Figure 3.6. Again, this relation is nearly linear, and also the load levels are again higher than those for the Type I and II specimens. Moreover, as for the previous types of specimens, total specimen failure occurred at about 30 to 45% higher values than those associated with initiated cracking. Some cracks which initiated near the free edge reached the edge as shown in Figure 3.7.

[1]Penetrant dye inspection is performed in the following steps:

1. The inspection surface is cleaned with s special solvent (McMaster-Carr Co.).
2. The dye is sprayed on after the specimen dries.
3. After allowing about 10 minutes for the dye to penetrate any surface cracks, the excess dye is removed with a cloth moistened with the cleaning solvent in step 1.
4. A developer is sprayed on, which turns white and draws the dye out of the cracks, forming red lines.

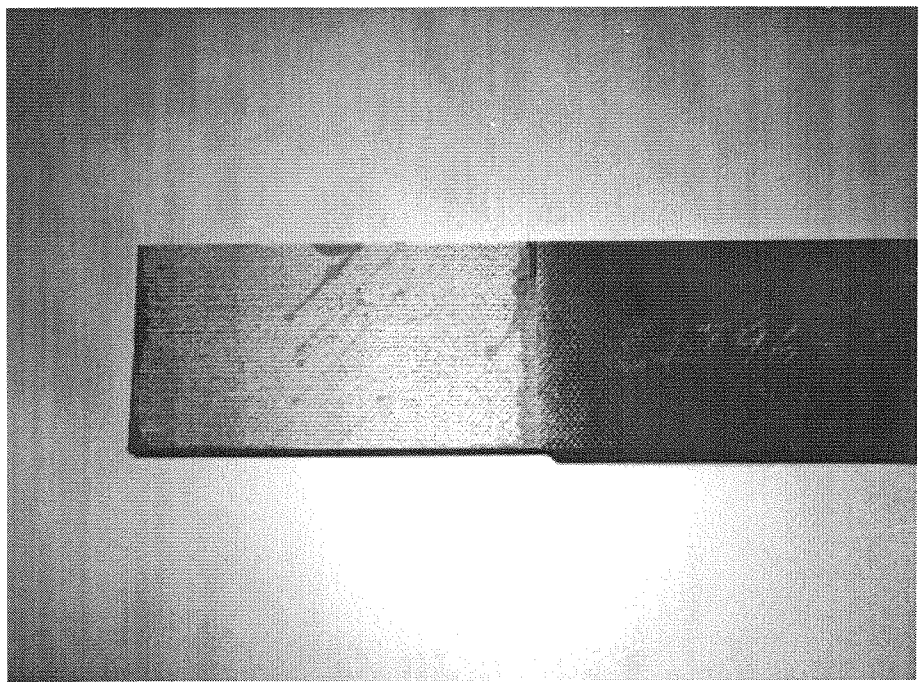

Figure 3.5: Cracks in Type III - Top view

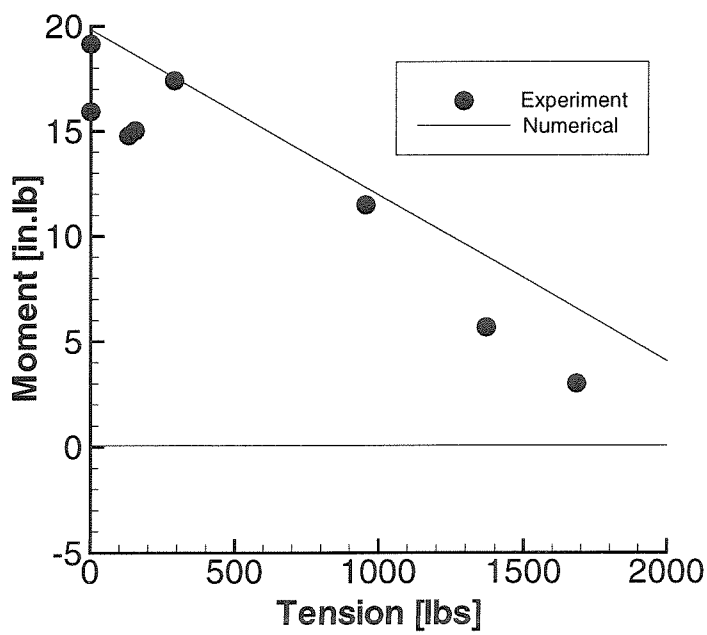

Figure 3.6: Failure loads of Type III

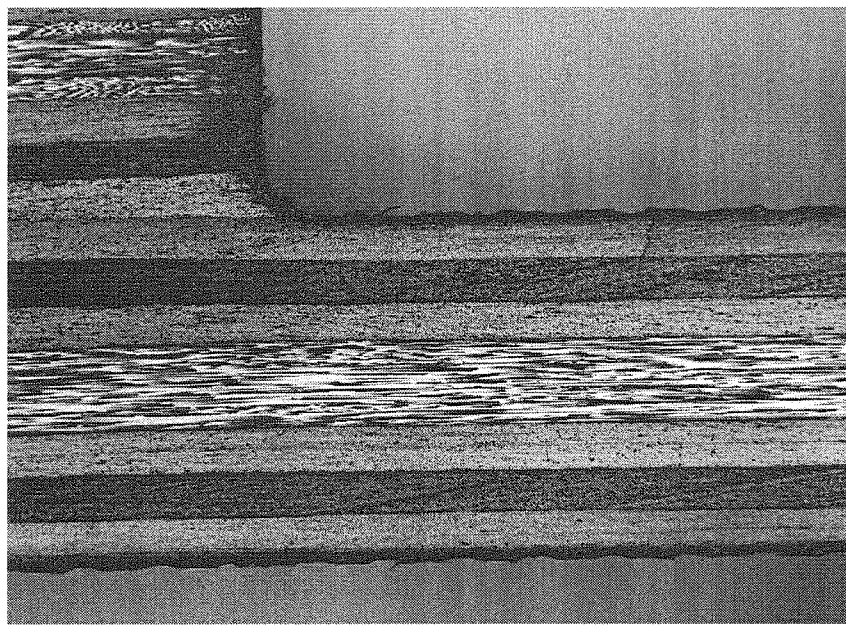

Figure 3.7: Side View of Type III specimen

3.3 Type IV Specimens

In this type of specimen the laminae adjacent to the interface possess only 0^o orientations so that cracking across the plate lamina is not favored. Instead, the failure occurs by delamination and fracture propagation. This is illustrated in Figure 3.8a, with the experimental interaction of moment and tension at failure initiation presented in Figure 3.8b. Disregarding again the analytically determined trace, the failure points present now a more nearly parabolic curve rather than a straight line, which is consistent with the different kind of failure mode observed. More importantly, the values of moments and tension at which failure is initiated is higher by a factor of about two, when compared with those for the Type I, II and III specimens, where trans-lamina fracture governed.

Another important difference relative to specimens of the I, II and III types arose in examining the residual specimen strength after initial delamination was observed: In the Type IV specimen, total failure followed the crack initiation process rather

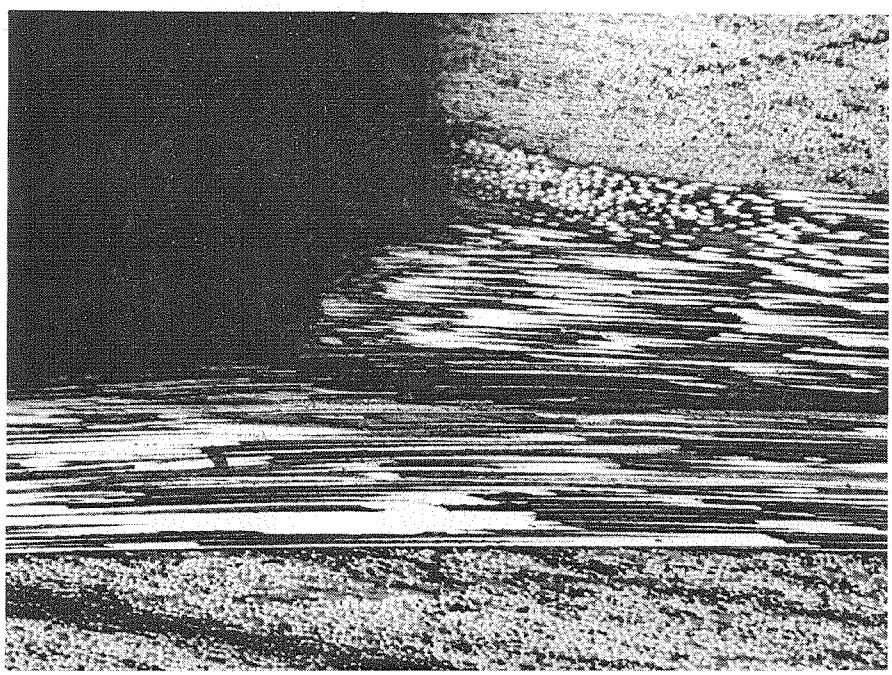

(a) Delamination

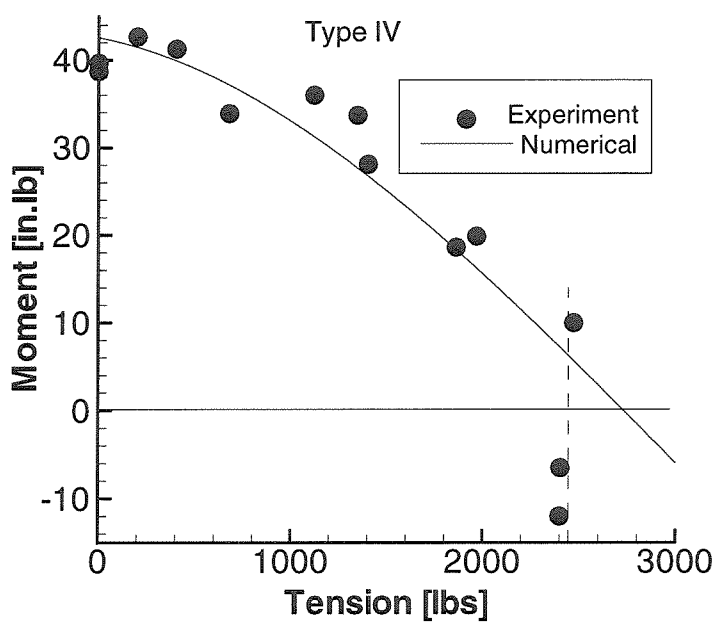

(b) Failure Loads

Figure 3.8: Type IV - Failure mode and load

Specimen	Test	Initiation moment	Propagation moment	Difference
Type 4	4-point bend	39.66 [lb-in]	45.84 [lb-in]	16%
	3-point bend	38.28	41.14	7%

Table 3.3: Comparison of delamination initiation and propagation moments - Type IV

closely, so that there was a "safety margin" of only about 10% that separated initial and total failure (see Table 3.3). After exceeding the failure initiation, the initial delamination crack propagated further and opened more as shown in Figure 3.9. The propagation was catastrophic as much of stiffener separated from the plate.

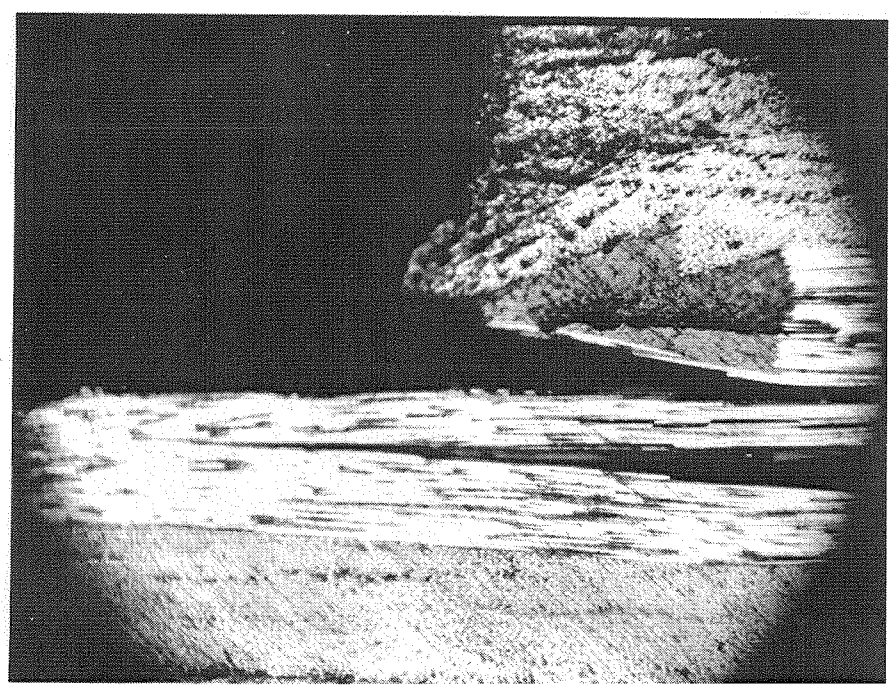

Figure 3.9: Crack propagation - Type IV

Chapter 4 Finite Element Analysis

4.1 Finite Element Model

A rationale for the failure behavior described in the previous chapter was developed by means of a finite element analysis with the commercial program ABAQUS. We take guidance from the apparently different characters of the moment/tension interaction curves and examine the failure behavior for specimen Types I, II, and III in terms of ply cracking, and that of Type IV as governed by delamination fracture.

It was clear from the detailed physical observations that the corners of the specimens, though carefully prepared for this study, were not very sharp[1], and that failure initiation did not occur at the radius proper (see Figure 3.2, as well as the discussion in section 3.1). Accordingly, it was not deemed necessary to address this problem with a singularity in mind and that the element mesh did not need to be extremely small in the neighborhood of the corner.

Specimens as loaded by the two frames were modeled as shown in Figure 4.1. The model involved over 13,000 degrees of freedom for the base problem which was analyzed on a Cray 90. The size of problem (degrees of freedom) was limited through the use of incompatible elements and nonlinear analysis. For reasonable results around the corners, the shaded part of the two meshes was refined further and solved by using the submodeling technique.

Submodeling is a technique of studying a local part of a model with a refined mesh, based on interpolation of the solution from an initial, global model, onto the nodes on the appropriate parts of the boundary of the submodel [14]. The submodel has 1,200 elements and 7617 nodes (1617 user defined). After appropriate boundary conditions were given to the global models, the model was solved in nonlinear

[1]In terms of Kubr's analysis, "sharp" should be measured in terms of a radius of curvature that is very small compared to a lamina thickness.

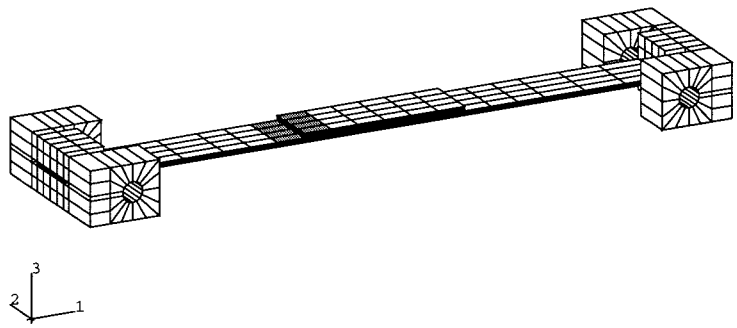

(a) Three- and four-point bending

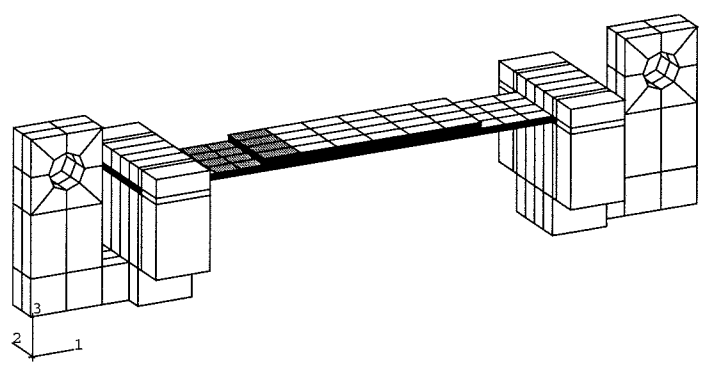

(b) Mesh for proportional loading

Figure 4.1: Coarse finite element meshes for the two loading devices (grey areas; domains for submodel)

geometric procedure and then the submodel was solved. The submodel is shown in Figure 4.2. Stress (or strain) components of the submodel were computed at the integration points of the elements with the aid of the commercial finite element analysis program ABAQUS. The C3D8I element used is a three-dimensional linear brick solid element with incompatible modes and has 8 integration points. Because of the 13 internal degrees of freedom, the elements are somewhat more "expensive" than regular displacement elements. But the elements have incompatible modes[2] to improve the result for the bending behavior [14].

The plies were assumed to be transversely isotropic material. Each of the plies is represented in the model by one element in the thickness direction. Because the deformations are large relative to the specimen thickness, kinematically nonlinear analysis is employed consistently. ABAQUS input programs are given in Appendix. Mechanical properties of a ply are listed in Table 4.1. The data were obtained by Lockheed-Georgia [21].

Another purpose of the finite element analysis is to examine the interaction of moment and tension at failure; i.e., to explain the experimental points in the tension-moment plane. Because of the complex nature of composite materials, it is not likely to obtain results with the same level of consistency as for materials which are isotropic and homogeneous. With composites there are many parameters that vary from one specimen to another, even when the specimens are cut from the same plate. A few of these parameters are fiber volume fraction; size and position of resin-rich areas, and impurities; positioning of the fibers relative to each other and relative to the step. In addition to those parameters, the shape of the corners may be important as well. As pointed out in the previous chapter, the corner is round, not a "sharp" 90°.

[2]Incompatible elements have incompatible modes to improve the bending behavior. In addition to the displacement degree of freedom, incompatible deformation modes are added internal to the elements. The primary effect of these degrees of freedom is to eliminate the so-called parasitic shear stresses that are observed in regular displacement elements if they are loaded in bending. The incompatible mode elements perform almost as well as second-order elements in many situations if the elements have an approximately rectangular shape. The performance is considerably less if the elements have a parallelogram shape. For trapezoidal element shapes, the performance is not much better than the performance of regular displacement elements.

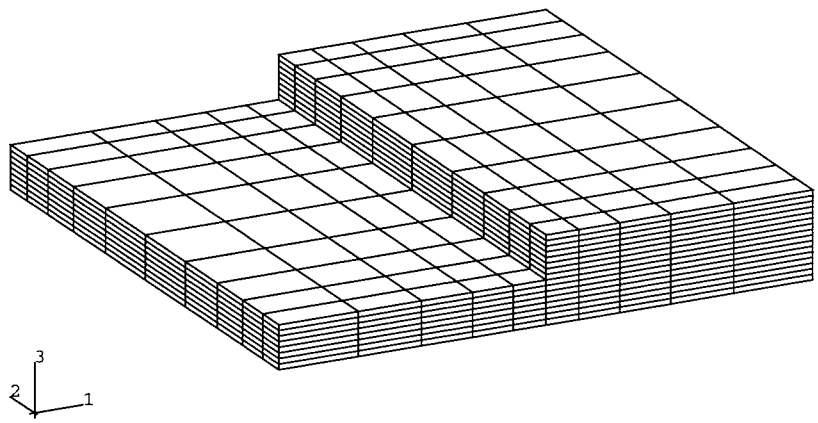

Figure 4.2: Submodel

Property	R.T. Dry	-67F Wet	160F Wet
E_{11}^T [Psi]	20.5×10^6	20.8×10^6	20.5×10^6
E_{22}^T [Psi]	1.67×10^6	1.70×10^6	1.35×10^6
G_{12}^T [Psi]	0.87×10^6	0.90×10^6	0.60×10^6
ν_{12} [Psi]	0.30	0.35	0.30
E_{11}^C [Psi]	18.5×10^6	19.5×10^6	19.5×10^6
E_{22}^C [Psi]	1.64×10^6	1.70×10^6	1.40×10^6
α_1 [in/in-F]	0.25×10^{-6}	0.24×10^{-6}	0.24×10^{-6}
α_2 [in/in-F]	16.2×10^{-6}	16.0×10^{-6}	16.2×10^{-6}
$\rho[lb/in^3]$	0.057		
$\epsilon^T(0^o - \text{Limit}^*)$	.00653	.00580	.00620
$\epsilon^C(0^o - \text{Limit}^*)$	.00670	.00630	.00620
$\epsilon^T(90^o - \text{Ultimate})$	.00500	.00480	.00380
$\epsilon^C(90^o - \text{Ultimate})$	.01000	.00900	.01000
$\mu_{xy}(\text{Limit}^*)$	.01330	.01330	.01330

Table 4.1: Mechanical properties of AS4/3502 single ply

Specimen	Experiment	Incompatible Element	Compatible Element
Type 1	8.79 [lb]	8.73	23.2
Type 2	7.76	6.90	
Type 3	5.17	4.92	

Table 4.2: The lateral forces from measurement and computation

Because of this variation, the points in the tension-moment plane are scattered. After the appropriate failure criterion is developed, the criterion is used to determine failure loads by numerical means.

The performance of the finite element model was checked by comparing the lateral forces from pure bending tests. In pure bending experiments, lateral force and deflection at the application of the force were measured. Then the deflection was given as input to finite element model to compute the lateral force. The two forces from experiment and computation are compared in Table 4.2. For Type I deflection at the point of load was 0.472[in] which is about 6 times larger than the plate thickness. The performance of the same model with the regular (compatible) element C3D8 is also shown in the table. For Type I, the force obtained with compatible elements was 2.6 times larger than the experimental results.

4.2 Type I and II Specimens

The typical strain distribution[3] in Type I specimen is shown in Figure 4.3 and 4.4 for two different loading conditions, where the strain components are given in directions relative to the fiber direction. Axis 1 is in the fiber direction, axis 2 is in fiber-normal, and axis 3 is in the thickness direction. The figures show the existence of a boundary layer [15] near the two free edges, $y = 0$ and $y = 1$. Note that in conforming with typical strength of materials concepts ϵ_{13}, ϵ_{23}, and ϵ_{33} almost vanish except near the

[3]The location of the points represented here are at integration points about 20% of the lamina thickness below the top surface of the plate.

free edge and along the corner.

Since for the lay-up considered here the failure is in the form of matrix cracking, this suggests that a strain or stress in the fiber-normal direction is the driver of failure. The numerical results evaluated for loads equal to those at failure initiation in the experiments showed that the maximum lamina strain ϵ_{22} was close to the ultimate strain ϵ_{ult} of a single ply ($\epsilon_{\text{ult}} = 0.005$). Thus loading conditions were changed computationally to determine those combinations of tension and moment for which the maximum ϵ_{22} was equal to the ultimate strain ϵ_{ult}. In Figure 4.5 and 4.6, the maximum strain ϵ_{22} is 0.005 for four different loadings on Type I and II, respectively. Note that the profile of the distribution is nearly the same for all loading combinations. We also note that the normal strains ϵ_{11} and ϵ_{22} achieve (small relative) maxima on the edge of the specimen, as depicted in Figures 4.3(a) and (b), which are not symmetric with respect to the specimen centerline (parallel to the tension axis). This small difference is sufficient to cause failure initiation consistently on one side of the specimen and at one specific corner (the specimen is rotationally symmetric); this fact made it possible to locally and systematically observe the failure initiation with a microscope.

The numerically determined failure load interactions are compared with experimental results in Figures 3.3 and 4.7. In spite of the (kinematically) nonlinear behavior of the specimen, the relation between the moment and the tension at failure is linear, as conjectured in section 3.1. Moreover, the figure demonstrates rather good agreement of the computations with the experimental results, indicating that a maximum lamina strain criterion can be used to estimate failure loads.

However, the maximum *strain* criterion can be replaced with a maximum *stress* criterion to predict failure loads. The maximum fiber-normal stress σ_{22} was equal to $\sigma_{\text{ult}} (= E_2 \epsilon_{\text{ult}} = 8350[\text{psi}])$ under the numerically determined failure loads in Figures 3.3 and 4.7.

The failure initiation of Type I and II specimens will be re-examined in section 4.5 in terms of a fracture mechanics concept, the energy release rate.

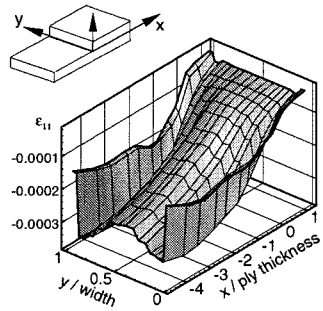

(a) ϵ_{11}

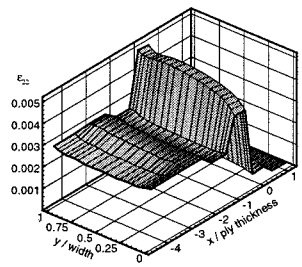

(b) ϵ_{22}

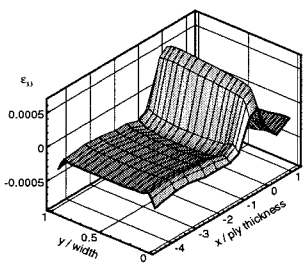

(c) ϵ_{33}

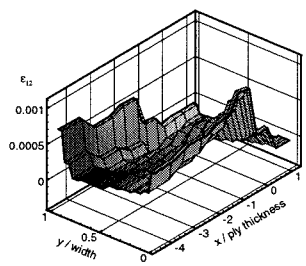

(d) ϵ_{12}

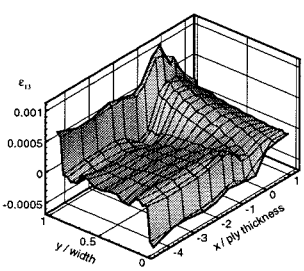

(e) ϵ_{13}

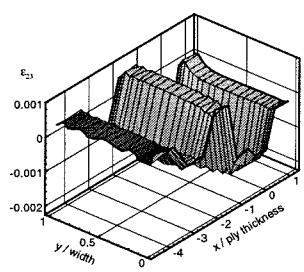

(f) ϵ_{23}

Figure 4.3: Strain distribution for T=520N (117lbs), M=1.6Nm (14.1in.lb) (The location of the points represented here are at integration points about 20% of the lamina thickness below the top surface of the plate.)

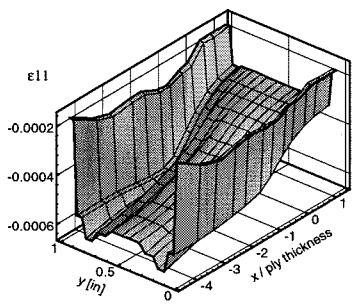

(a) ϵ_{11}

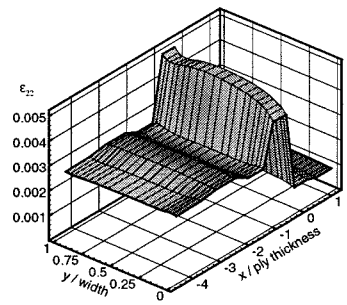

(b) ϵ_{22}

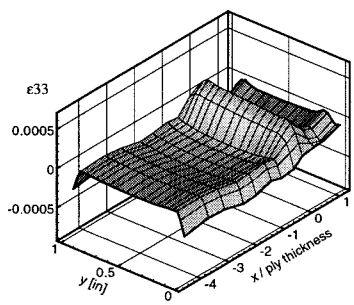

(c) ϵ_{33}

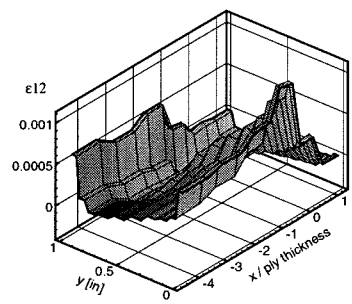

(d) ϵ_{12}

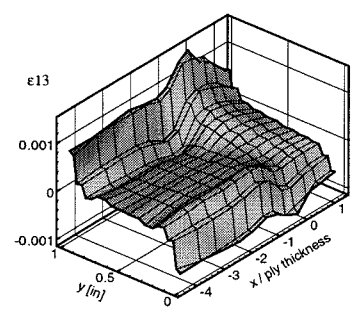

(e) ϵ_{13}

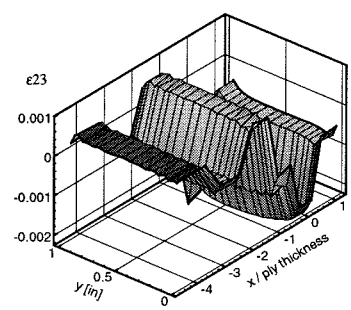

(f) ϵ_{23}

Figure 4.4: Strain of Type I - T=1165[lbs], M=5.63[lb-in]

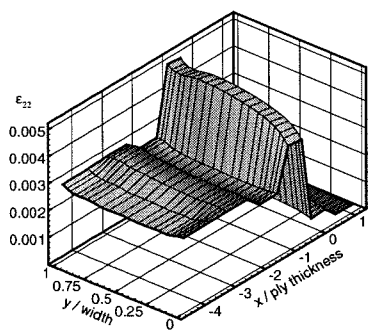

(a) T=520N (117lbs), M=1.59Nm (14.1 in.lb)

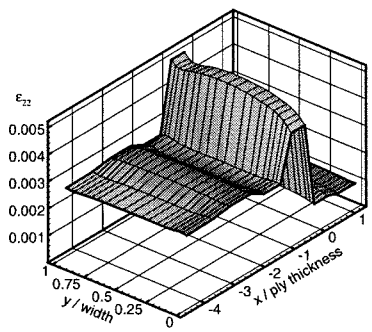

(b) T=5181N (1165lbs), M=0.63Nm (5.6 in.lb)

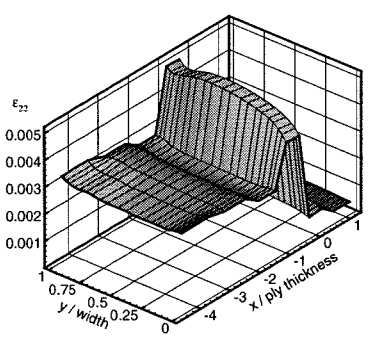

(c) T=1761N (396lbs), M=1.38Nm (12.2 in.lb)

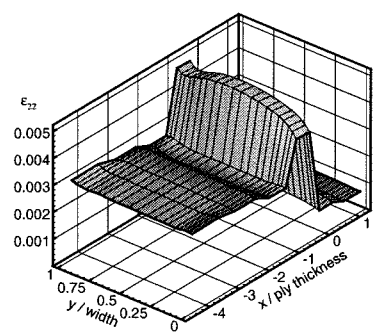

(d) T=3825N (860lbs), M=0.89Nm (7.9 in.lb)

Figure 4.5: Strain ϵ_{22} under different loading

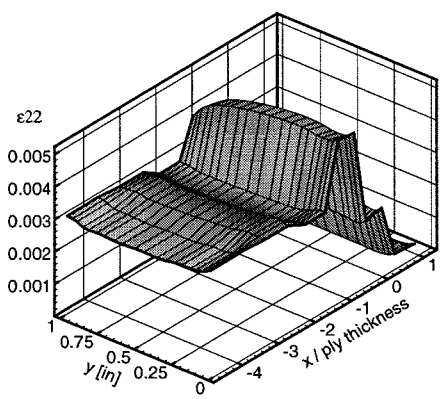

(a) T=113, M=16.0

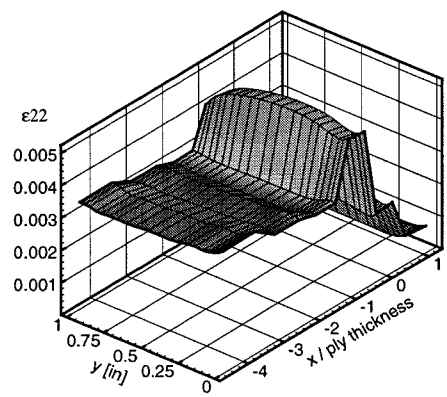

(b) T=575, M=12.4

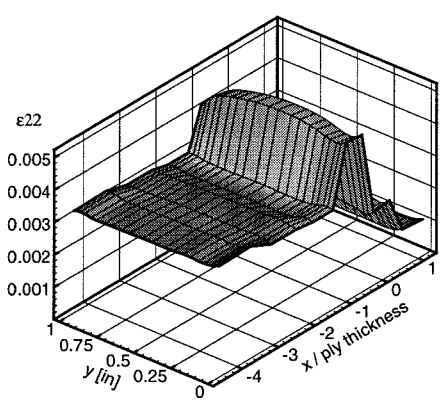

(c) T=1030, M=8.54

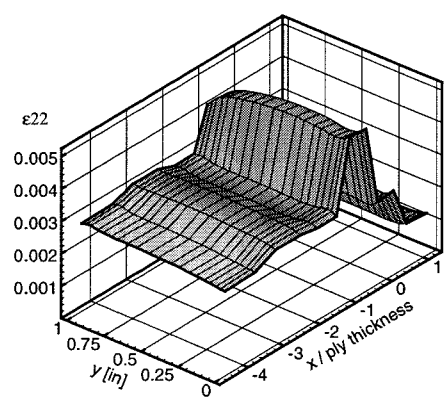

(d) T=1415, M=5.5

Figure 4.6: Strain ϵ_{22} of Type II

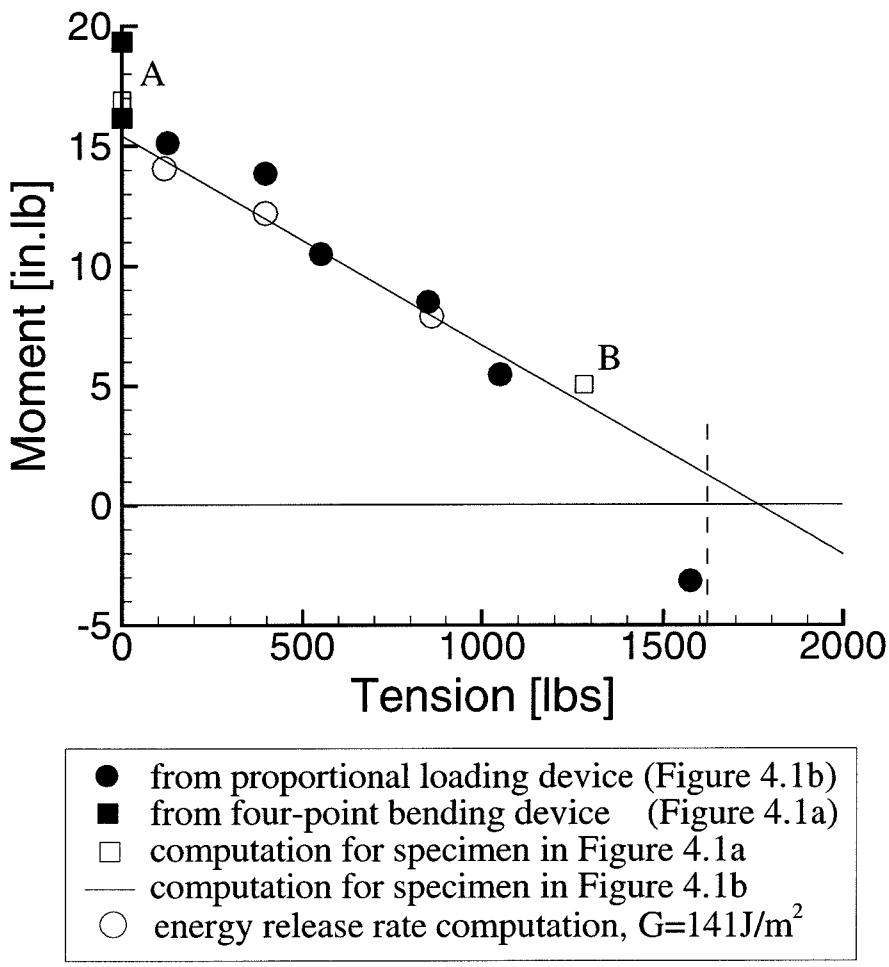

Figure 4.7: Failure loads from experiment and computation

In this context the question arises as to what the appropriate (minimal) size of the finite element near the corner is to be, because for a "mathematically sharp" corner, a continued reduction in the element size results in increasing locally computed stresses. This problem can, in principle, be circumvented by modeling the true curvature of the corner configuration and making the elements small with respect to the fillet radius. This approach, while correct for the particular specimen under consideration, does not address the generic problem of how to use computations for thickness discontinuities in design related issues. An alternate method is to size the elements in a manner that is typical for the problem at hand so that the analysis renders results that are consistently in line with the experiments. Accordingly, we chose to compute strains at integration points, with the distance of the integration point where the maximum strain was computed being about four times the ply thickness from the corner. This process introduces implicitly a (limiting) characteristic length into the analysis, which has been advocated repeatedly before in the failure analysis of laminated composites containing (potential) singularities or stress concentrations ([8], [16]).

Two computation models are presented in Figure 4.1, both employing the same ultimate ply strain. Because of the large deformations and the fact that coupling between tension, bending and torsion could not be completely eliminated in the tests, there exists a dependence of the load level on the length of the specimen. The square symbols in Figure 4.7 are derived from the long specimens tested in the MTS-driven device (*c.f.* Figure 4.1 a) and the round ones from the short specimen tested in the combined loading frame (Figure 4.1 b). Accordingly, computations were performed to conform to these situations. In Figure 4.7 the straight line represents conditions derived for the "shorter" specimens (Figure 4.1 b). Computations for the longer specimens required slightly larger load levels and yielded the open square symbols designated as points A and B. The finite element analysis supports thus the experimental findings.

4.3 Type III Specimens

The typical stress distributions are shown in Figures 4.8 and 4.9. The magnitude of σ_{12} are comparable to σ_{22} so that interaction of the two components should be accounted to predict failure. For Type III specimens, the Tsai-Hill criterion was applied to account for the effect of the in-plane shear stress.

Many theories have been developed to predict strength under general states of stress. The Tsai-Hill criterion is widely quoted in composite textbooks and is often used in laminate analysis programs. The theory is based on Hill's theory for ductile anisotropic materials and adapted to the more brittle heterogeneous composites. The Tsai-Hill criterion is given in equation (4.1). Failure does not occur when the left-hand side is less than unity.

$$\left(\frac{\sigma_1}{\sigma_{1u}}\right)^2 + \left(\frac{\sigma_2}{\sigma_{2u}}\right)^2 - \frac{\sigma_1\sigma_2}{\sigma_{1u}^2} + \left(\frac{\tau_{12}}{\tau_{12u}}\right)^2 \geq 1 \tag{4.1}$$

where σ_{1u}, σ_{2u}, and σ_{12u} are failure (ultimate) stresses.

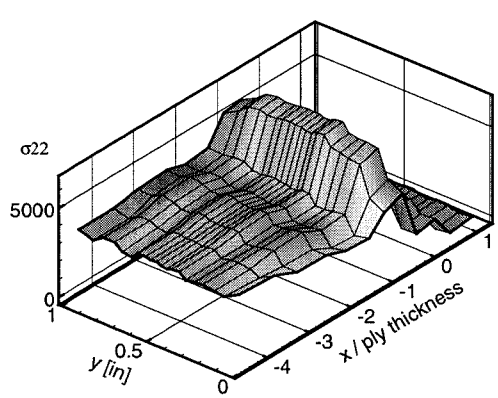

(a) σ_{22}

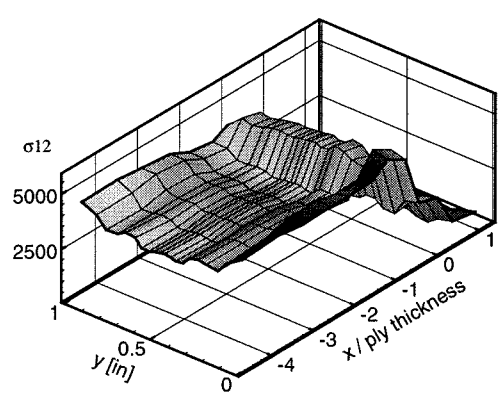

(b) σ_{12}

Figure 4.8: Stress distribution of Type III - T=132.[lbs], M=18.8[lb-in]

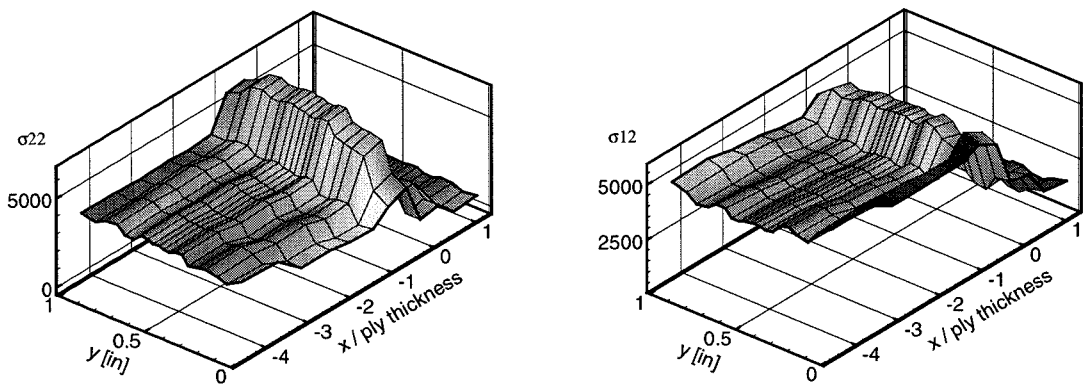

(a) σ_{22} (b) σ_{12}

Figure 4.9: Stress distribution of Type II - T=1105.[lbs], M=12.5[lb-in]

For the analysis in section 4.2 for Type I and II specimens, the second term in equation 4.1 is dominant. Then, the Tsai-Hill criterion reverts to the maximum stress criterion, $\sigma_2 \geq \sigma_{2u}$. Thus the result in section 4.2 can also be obtained by using the Tsai-Hill criterion.

4.4 Type IV

To examine the delamination failure in the Type IV specimens, an energy release rate criterion was applied. The concept of the energy release rate arises typically in fracture mechanics problems where it is associated with the propagation of a pre-existing crack by an arbitrarily small (infinitesimal) growth step. In the present study the inititial geometries are all considered to be crack-free, so that, strictly speaking, energy release rates are not defined. However, this concept is applied to situations where a small but finite crack length is generated from an initially crack free geometry, and this discrete process is referred to as the energy release rate procedure.

The procedure for determining the energy release rate G was similar to the finite element formulation of a crack closure integral technique employed by Rybicki et al. [17]. Two submodels, one with and one without a delamination crack were analyzed (using the same boundary conditions), and the difference between the total strain energies of the two models was determined to represent the energy release rate G. The delamination was modeled by using coincident nodes along the corner edge of each element across the width of the specimen along the thickness discontinuity. A deformed shape of the submodel with a crack is shown in Figure 4.10. A typical distribution of the interlaminar normal stress σ_{33} is shown in Figure 4.11 for the submodels with and without crack under the same loading condition. It is easily seen that the stress σ_{33} in the submodel with the crack is relaxed.

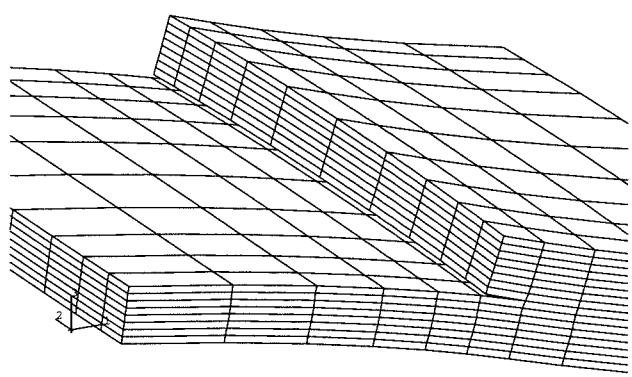

Figure 4.10: Deformed shape of a submodel with a crack

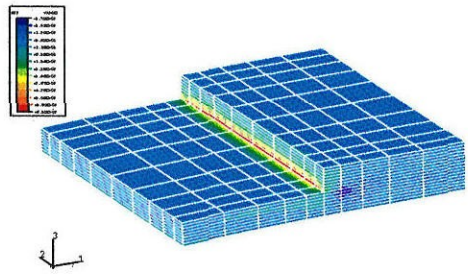

(a) Without crack

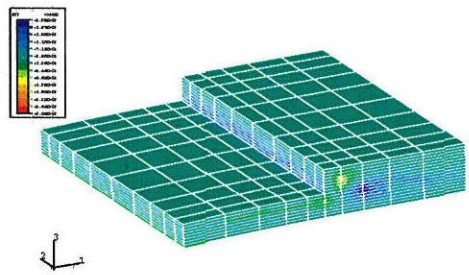

(b) With crack

Figure 4.11: Contour plot of σ_{33} in Type IV - M=41.35[in.lb], T=220lbs

The strain energies of each element were added to give the total strain energy of the model. Because the fibers across the "interface" were oriented in the same direction, the delamination was not a true interfacial separation, so that questions related to interfacial fracture mechanics did not arise. As a result the potential problem of mesh size for interfacial fracture did not pose a problem.

The curve in Figure 4.12 has been computed for a constant value of $G = 212 J/m^2$. Whitney *et al.* (1982) had shown that for AS4/3502 composites the critical mode I interlaminar energy release rate was $G_{Ic} = 161.1 J/m^2$ $(0.92 lb.in/in^2)$. Thus the present analysis is reasonably consistent, if not identical, with earlier, similar measurements on different geometries, which lends additional credence to the observation that Type IV specimens fail according to a fracture/delamination criterion.

It is of interest to recognize that there are numerous earlier studies devoted to the determination of interlaminar stresses for failure estimation. In cases where the interfacial failure is of a mixed mode type, stress or strain criteria are generally not very useful. In order to examine whether this situation prevails here, we examine in Figure 4.12 predictions of failure in terms of exceeding either the stress σ_{33} or the strain ϵ_{13} and compare it to the correlation of the data by a constant energy release rate G. It is clear that the latter is in better agreement with the data than the stress or strain criteria: The computed maximum strains normal to and across the fibers were significantly smaller than the failure strains.

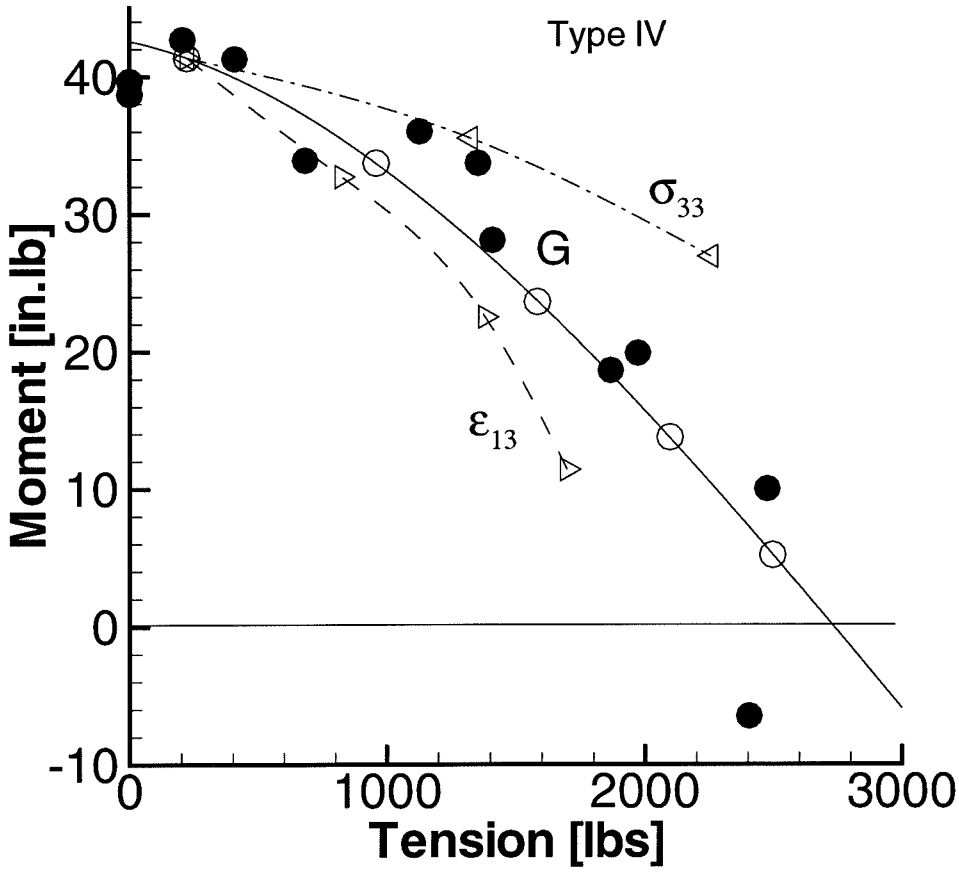

Figure 4.12: Application of interlaminar stress and strain criteria

Two questions arise in the context of intralaminar fracture, namely (a) what role does a different (finite) crack initiation size step play, and (b) what is the effect of nominal shear along and tension across the failure zone, which is referred to in standard interface fracture as the mixed mode problem. We note for clarification that while we have referred to an "interface" between laminae adjacent to the step, this is not an interface in a physical sense; specifically, for specimens of Type IV that "interface" is really in the center of the two identically oriented laminae that belong each to the plate and to the step, respectively.

The effect of different fracture step sizes can be examined in Figure 4.13 where the energy release rate is computed for different crack initiation lengths such that the prediction fits on the same curve in Figure 3.8. It is clear that the variation is rather small and it can be shown that it is considerably smaller than the experimental data scatter.

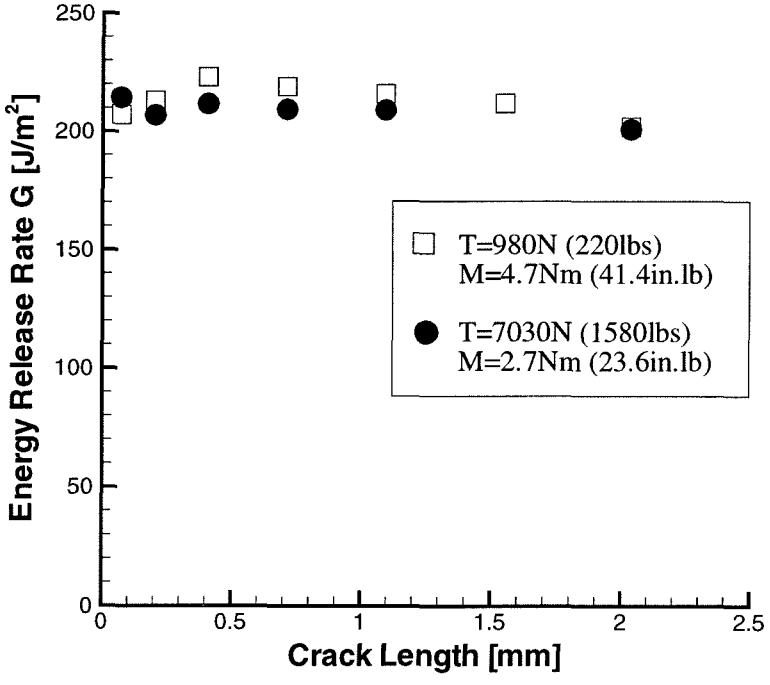

Figure 4.13: Crack length vs. Energy release rate for Type IV

We address next the role of mode-mixity. While it may not be fair to include this concept in the present discussion because, again there is no initial crack present, and not even a physical stress singularity at the base of the step, the fact that the energy release rate for this type of failure is distinctly different from those for the previous failure modes justifies this examination. Because there is no stress singularity, the standard description of a mode mixity in terms of stress intensities is not appropriate and we use, instead, stress ratios ($\tan^{-1}(\sigma_{13}/\sigma_{33})$) from the high stress region at the base of the step. If one compares that value with the data from mode mixity experiments [23], one finds that this ratio falls well within the (flat) region where the fracture energy is insensitive to mode mixity effects.

4.5 Energy Release Rate Computations - Type I, II and III Specimens

Having demonstrated that the failure initiation for specimens of Type I, II and III can be "explained" in terms of laminar maximal stress or strain arguments (sections 4.2 and 4.3), it has also been shown that such is not the case for specimens of Type IV, where fracture propagation parallel to the fibers dominates. However, in the interest of exploring a **common** failure description for all failure initiations, let us re-examine the previous failures also in fracture mechanics parlance. One finds that all failures can be described in terms of a common fracture principle, which for the previously considered lay-ups yield the same results; for these situations the stress or strain criteria are interchangeable with the fracture energy computations as outlined below, provided one allows for different values of associated fracture energies.

One question that arises naturally concerns the lenth of the crack generated under these circumstances. For specimens of Type IV this issue has been considered in connection with Figure 4.13. For specimens of Type I, II and III this question warrants further discussion.

4.5.1 Type I and II Specimens

In the case of trans-laminar fracture in Type I and II specimen the crack typically appears "suddenly" across the whole lamina thickness and across the whole specimen width. It is thus natural to accept the lamina thickness as the prevalent crack extension dimension.

Figure 4.14 demonstrates the appearance of a crack (model) at the base of the step. The question is whether the introduction of such a crack through the lamina thickness yields essentially the same result as the lamina maximum strain criterion used to generate the straight line in Figure 4.7. The answer is affirmative for Figure 4.7 if the fracture energy is taken as $140.5 J/m^2 (0.8 lb/in.)$.

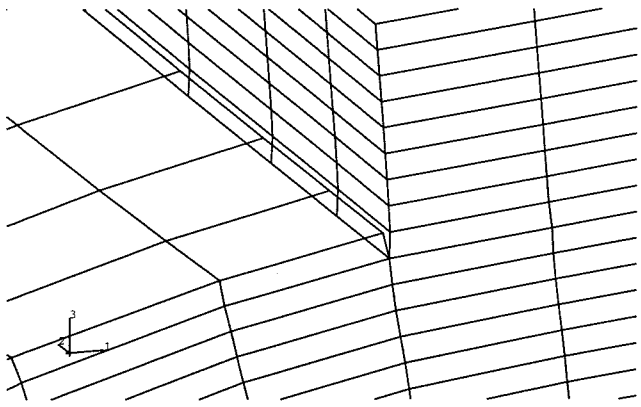

Figure 4.14: Deformed shape of a submodel with a matrix crack for specimens of Type I and II

4.5.2 Type III Specimens

The submodel with a matrix crack in Type III is shown in Figure 4.15. For this specimen type multiple cracks appeared in the "top lamina" of the plate oriented at 45^{o} with respect to the specimen axis (parallel to the fibers). The length of these cracks was about 30 times the thickness of the lamina (1/4mm ; 0.010in). Accordingly computations were carried out with a single crack of different lengths e ($5t \leq e < 30t$, t=lamina thickness) with the result that

a) the energy criterion produced the same straight line interaction between tension and moment as the Tsai-Hill criterion as shown in Figure 3.6; and

b) the energy release rate was insensitive to crack length in the stated range, but amounted only to $15 J/m^2$ for the single crack.

It is clear, however, that for this type of specimen the evolving crack geometry is not identified as clearly as for the other configurations, so that a practical use of the energy criterion is in doubt.

A submodel with a matrix crack in a Type III specimen is shown in Figure 4.15.

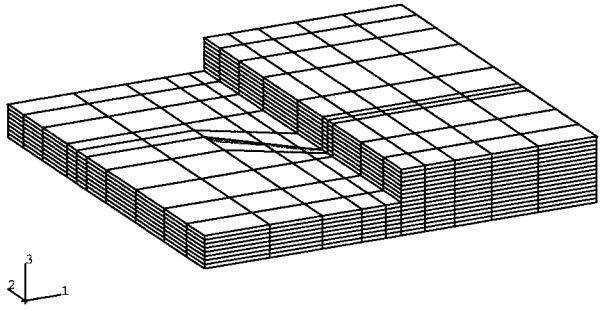

(a)

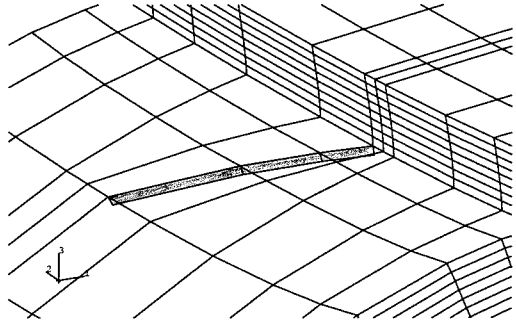

(b)

Figure 4.15: Submodel with a crack - Type III

Chapter 5 Effect of Elevated Temperature

5.1 Introduction

In composites four types of matrices are used: polymeric, matallic, ceramic, and graphite. The most commonly used matrices are polymeric. However, one of major potential shortcomings of the polymer matrix composites is that mechanical properties of the polymer are sensitive to elevated temperatures. As aircraft speeds increase, temperatures due to aerodynamic heating changes character of structural problems from mostly time independent to time dependent behavior. Thus the changes associated with failure modes engendered by elevated temperatures becomes as important part of the future design and engineering analyses of advanced and new aircraft.

In the previous chapters, failures at thickness variations have been examined for room temperature conditions. The same experimental and numerical procedures were performed to investigate failures under elevated temperatures. The combined loading frame and specimens were placed in an environmental chamber as shown in Figure 5.1. Two temperatures, 100^oC and 150^oC, were selected considering that the glass transition temperature T_g of the matrix is reported as 198^oC[1] (388^oF).

Experimental procedures for high-temperature tests were the same as those at room temperature except for the failure detection method. It was, at least initially, desired to observe the failure initiation under magnification inside of a thermal control chamber in spite of intervening class panes. This objective was pursued by constructing an optical set-up, essentially with the help of long-focal lenses ($f = 30cm$), to form a virtual image of the specimen surface external to the temperature cabinet; this virtual image could then be examined and enlarged through microscope obser-

[1]The temperature 93^oC is often quoted as a lower limit for continuous use temperature requirement for civil aircraft. This requirement rises to about 180^oC for skins of supersonic jets and military fighter aircraft.

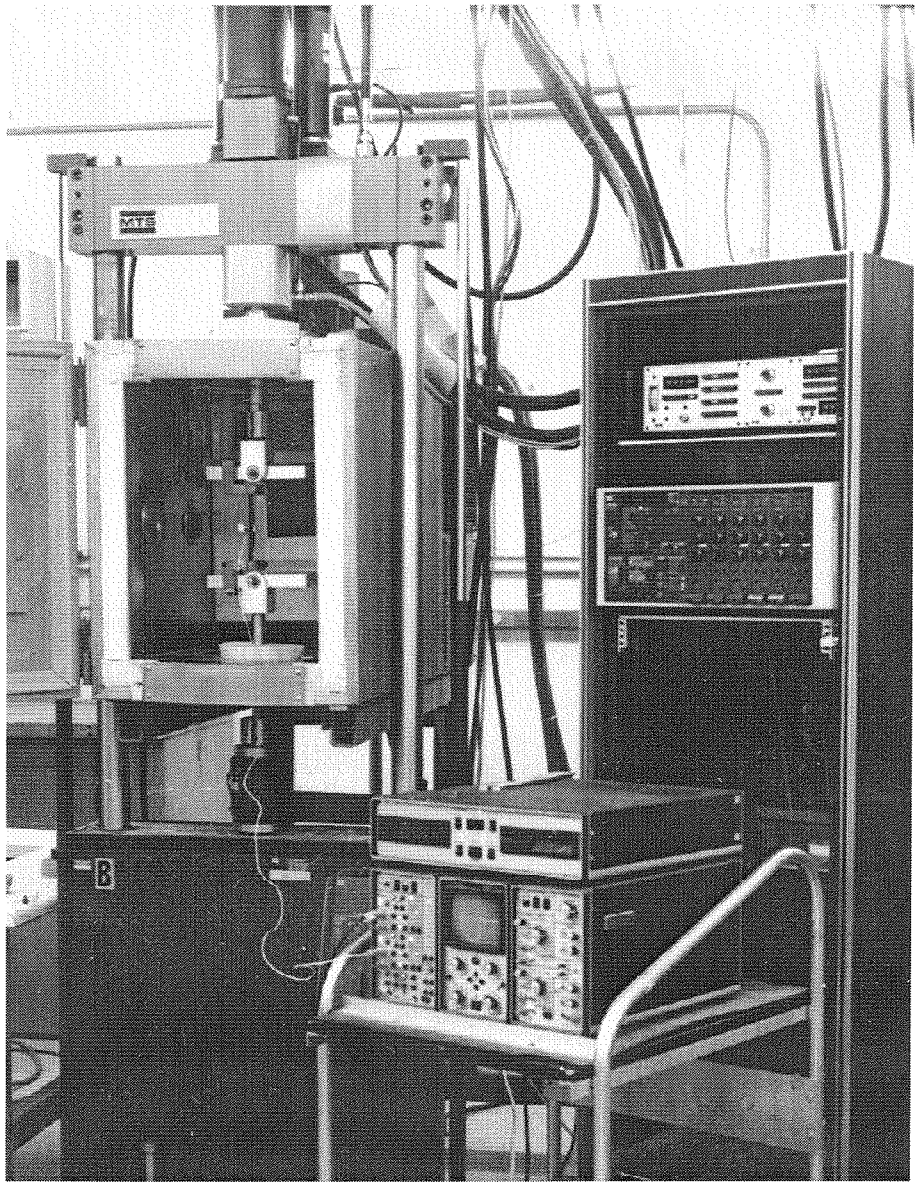

Figure 5.1: Experimental setup for high-temperature tests

Property	250F Wet	265F Dry	265F (130C) Wet
E_{11}^T [Psi]		20.0×10^6	20.6×10^6
E_{22}^T [Psi]			1.04×10^6
G_{12}^T [Psi]	0.14×10^6		
$\epsilon^T(90^o$-Ultimate)			.00344

Table 5.1: Mechanical properties of AS4/3502 single ply at high temperatures

vation. It turned out, however, that with this optical arrangement it was too difficult to locate and track the corner of the specimen practically and to focus on it so as to follow failure that might contain a creep or time-related effect. Instead of this microscope method, the acoustic emission method was then used to detect the initiation of failure because the correlation between acoustic emission and crack appearance had been established in numerous tests at room temperature.

The finite element analysis accompanying the high temperature experiment accounted for both the mechanical loading as well as for temperature induced stresses, assuming the specimens to be stress-free at 25^oC. Changes in the mechanical properties with temperature were also taken into account. Because the modulus in the fiber direction is dominated by the fibers rather than by the matrix, that modulus remained unchanged. The matrix dominated properties (transverse and in-plane shear modulus) were provided at 100^oC and 150^oC, but the latter (transverse and shear modulus) were available only for 1% moisture content (see Table 5.1). Properties were assumed to vary linearly with temperature in this range.

Because moisture generally has a deleterious effect on properties in addition to that derived from elevated temperatures, a parameter study for different stiffness values was carried out to access the sensitivity of the final result to this variation. This sensitivity study established that reasonable variations left the analytical results essentially unaltered, with a variation smaller than the experimental scatter could allow.

The mechanical properties at high temperatures [22] are given in Table 5.1.

Acoustic Emission

Acoustic emission is the name given to transient mechanical waves which are spontaneously generated by abrupt, localized strain changes within a body. In composites, acoustic emission is generated by cracking of the matrix, debonding of the matrix from the fibers, laminate seperation, fiber pullout and breakage of the fibers [20]. Under stress condition, an acoustic emission source is created that generates mechanical waves in the structure. These waves are detected by sensitive piezoelectric transducers attached to the surface by which they are transformed into electrical signals. The signals are then filtered, amplified, and analyzed.

For the current experiments, a 6mm (0.25in) diameter AE transducer (Micro-30, Physical Acoustics Corp., Princeton, New Jersey) was coupled to the specimen face using a special holder and vacuum grease for the couplant (see Figure 5.2).

A couplant is used to obtain a good contact, thus ensuring a better elastic wave transmission. The transducer is tuned to resonate at approximately 150 kHZ. The electrical signal from the sensor was monitored with an oscilloscope. When acoustic emission was detected, the signal triggered the oscilloscope to record the signal and load (see Figure 5.1).

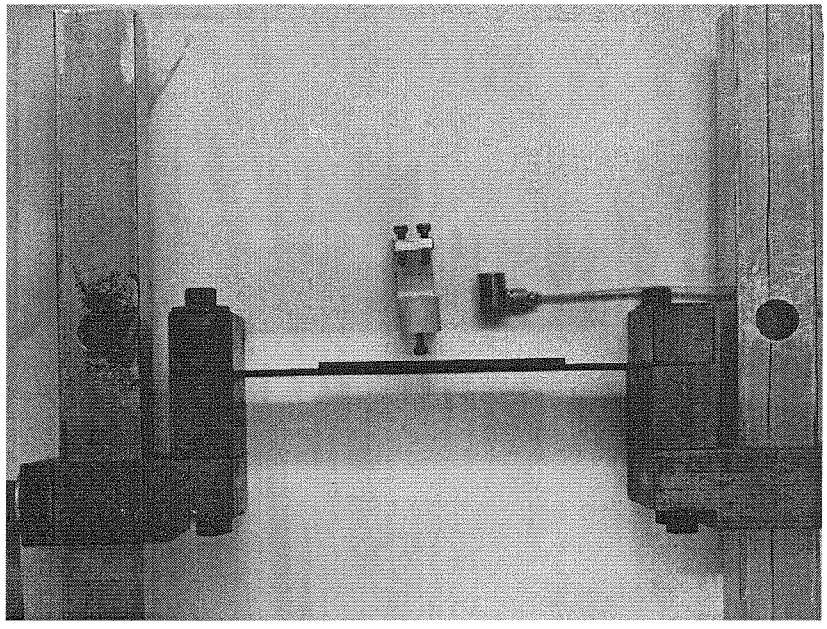

(a)

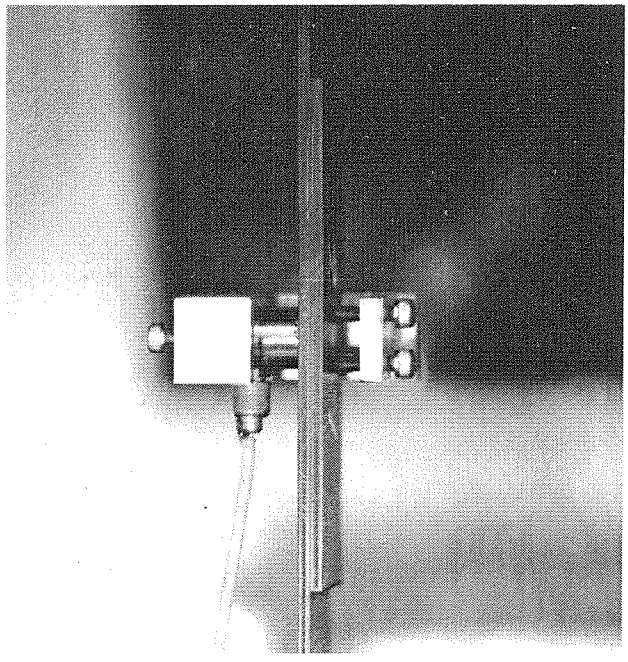

(b)

Figure 5.2: Acoustic emission transducer and holder

5.2 Type I and II Specimens

Specimens of Type I and II tested at $100°C$ exhibited failure characteristics identical to those at room temperature: The failure mode occurred again by matrix cracking. However, the magnitude of the failure loads were lower than those at room temperature (see Figure 5.3). The failure loads for the Type I and II specimens were so close to each other that the results are treated as the same. Again, a maximum strain failure criterion was used to compute the failure loads; however, a smaller failure strain (0.0038) was consistent with the data at $100°C$. We deplore again that a lack of sufficient test material precluded to explore the failure behavior of all types of specimens more freely at those temperatures.

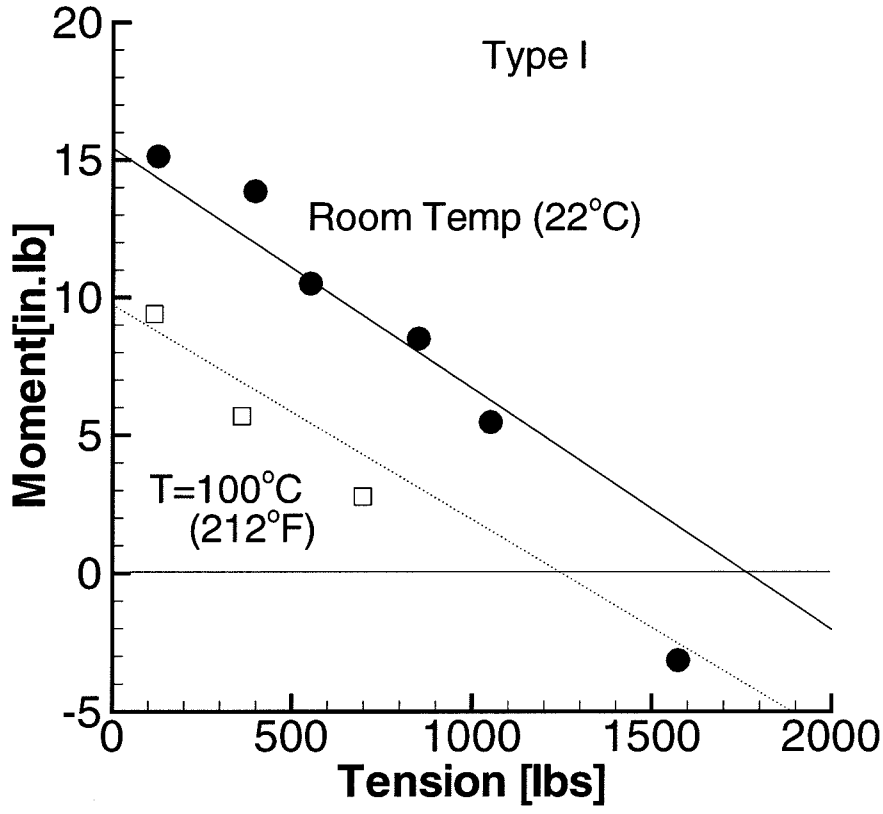

Figure 5.3: Failure curves of Type I at room and at high temperature

A typical acoutic emission signal is shown in Figure 5.4. The first failure event produced a pronounced acoustic signal, which decayed rather rapidly. The amplitude of the acoustic signal was of no particular concern in this study. Further analysis of the acoustic emission signal was not performed because the method was aimed only to detect any failure occurrence.

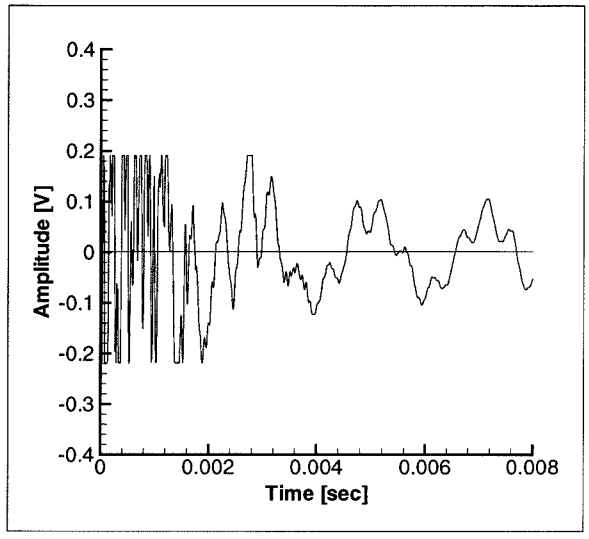

Figure 5.4: Acoustic emission signal - Type I, $100°C$

5.3 Type IV Specimens

Again, as for specimens of Type I and II, the failure loads at elevated temperatures for this specimen type were lower than those obtained at room temperature. However, the relative differences are now smaller as may be deduced from Figure 5.5. The finite element analysis was carried out to compute the failure loads by applying the same fracture criterion and computational procedure as for the analysis at room temperature. The critical energy release rates at $100°C$ and $150°C$ are 161 and 125 J/m^2, respectively. This critical energy value drops thus by about 0.68 J/m^2 per degree C. Though the material properties derived from wet specimens have been used in the computations, the above results are reasonable for dry specimens because

the energy release rate was not sensitive to commensurate changes in the transverse and shear moduli: If one were to allow the room temperature moduli to prevail at the elevated temperatures, one would find an energy release rate that is only 6% higher than that derived from the stiffness degraded by temperature (and moisture).

Acoustic emission signals at the two high temperatures are shown in Figure 5.6 and 5.7. The magnitude of the signal at $100[^{\circ}C]$ seems to be larger than that at $150[^{\circ}C]$.

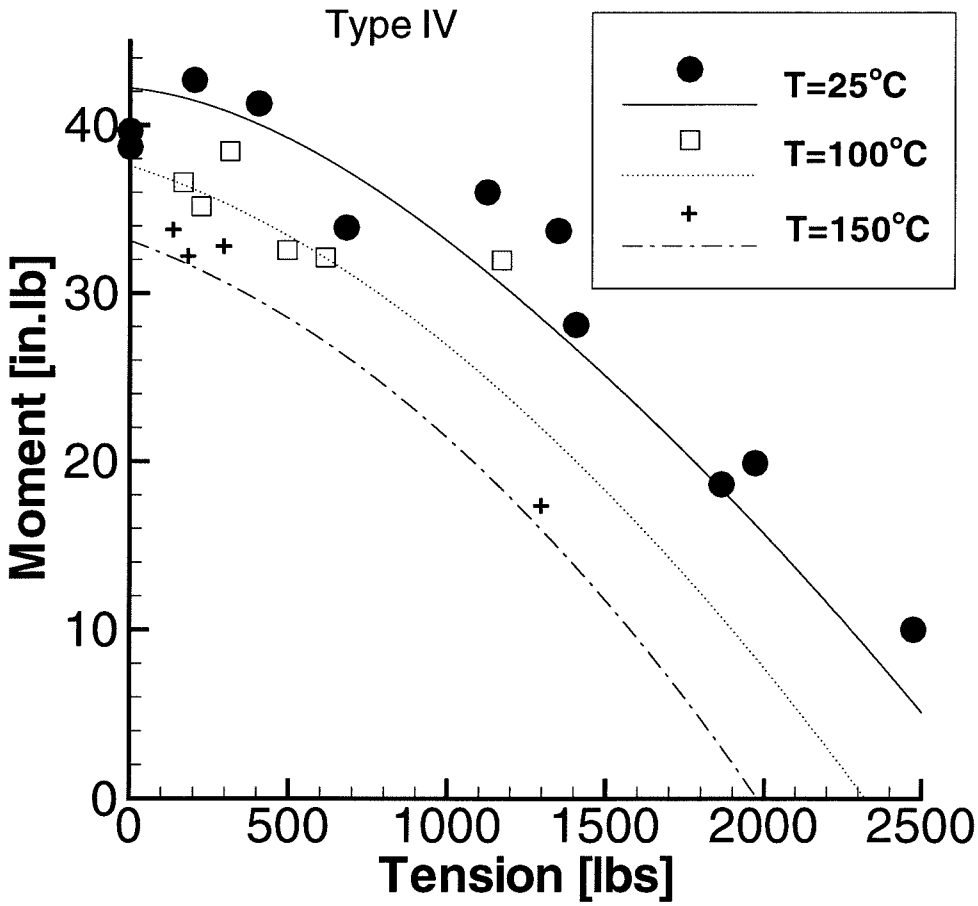

Figure 5.5: Failure curves of Type IV room and high temperatures

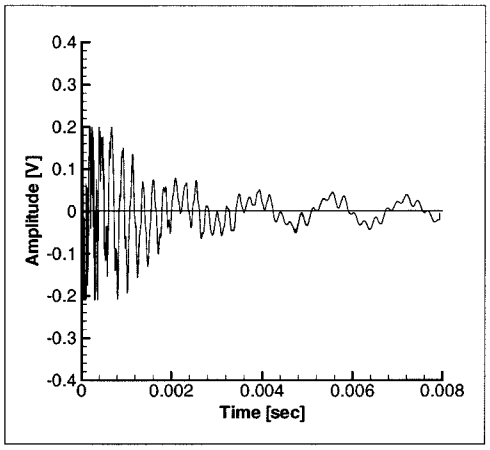

(a) T=224, M=35.2

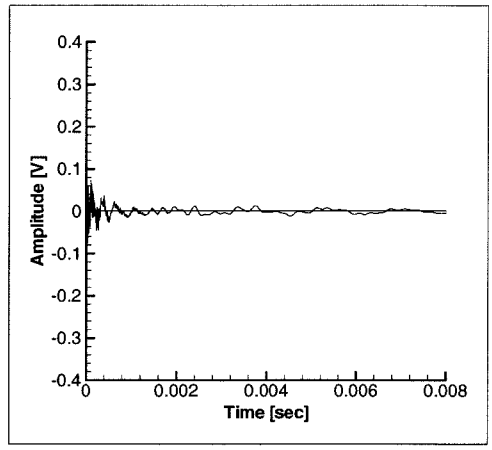

(b) T=494, M=32.6

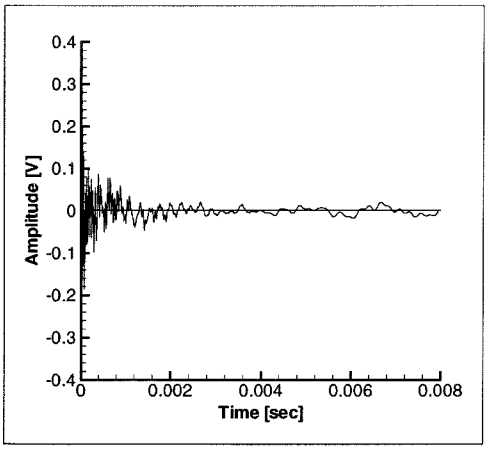

(c) T=613, M=32.1

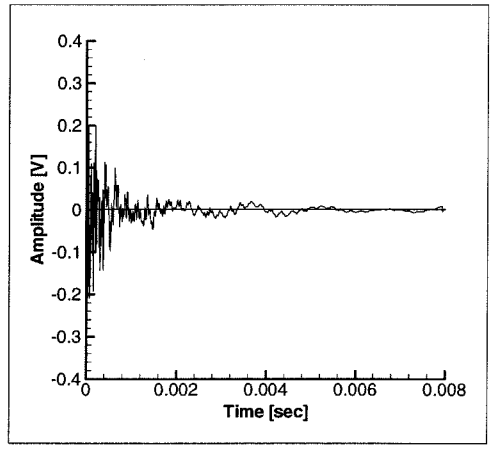

(d) T=1170, M=31.9

Figure 5.6: Acoutic emission signals - Type IV, 100[^oC]

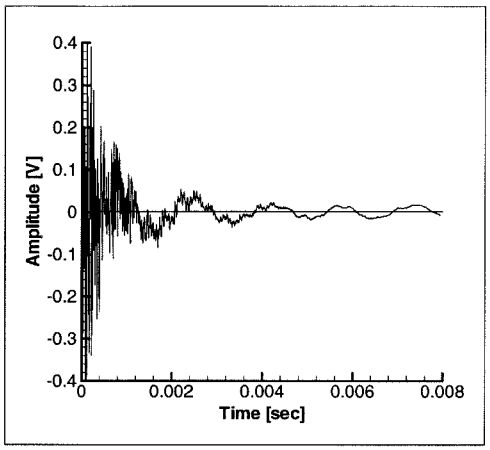

(a) T=138, M=34.

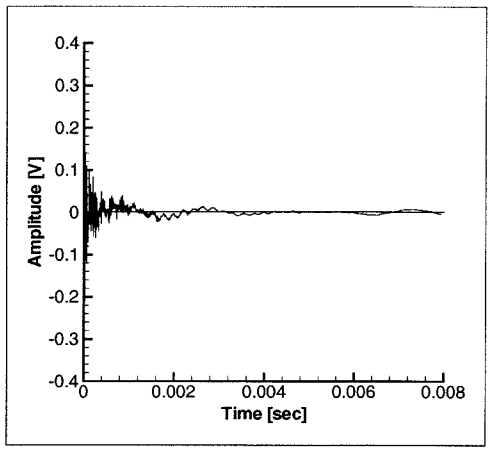

(b) T=184, M=32.4

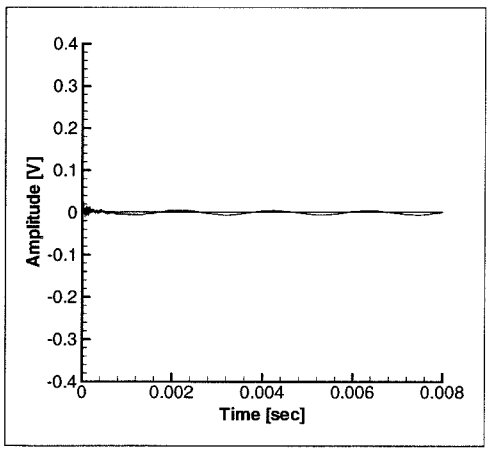

(c) T=297, M=33.

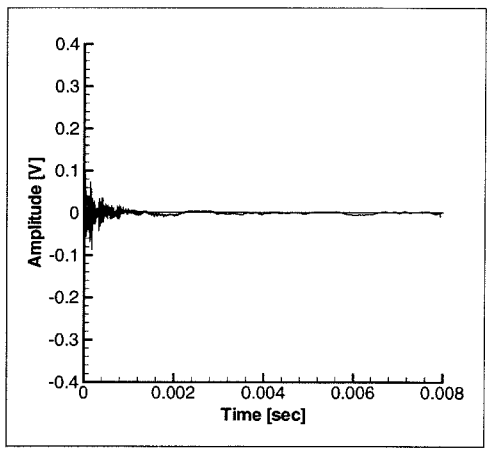

(d) T=1298, M=17.5

Figure 5.7: Acoutic emission signals - Type IV, 150[^oC]

Chapter 6 Conclusion

The failure initiation in laminated composites containing "sharp" corner has been studied experimentally and corresponding numerical evaluations are presented. Even though a lack of additional test materials limits the experimental data pool, clear observations and results emerge from this study.

Two distinctly different failure modes arise in the four stacking sequences encountered in this study: When the interface between the steps is contained between two layers of zero-oriented fibers (specimen Type IV), a delamination-type failure results which is best analyzed in terms of an energy release rate concept (fracture mechanics). The other configurations (specimen Type I, II, and III), containing fiber orientations on either side of the interface that have an orientation component deviating from the zero direction (by 45^o or more), fail by ply-fracture normal to the fiber orientation in the top ply of the "plate." Subsequent failure progression is by ply delamination and additional ply fractures.

While the appearance of sharp corners invites analyses in terms of stress singularity, this study shows [see again Kubr [10] and Gortsema [11]] that fillet-like geometries resulting inadvertently from any manufacturing processes call for evaluations employing non-singular stress field analysis. Accordingly, finite element computations, relying on discretization with lamina thickness as the dimension governing element sizes, appear quite adequate. Moreover, with a view towards design related issues, this type of analysis provides sufficiently accurate descriptions of the failure initiation process.

In spite of the large deformations observed, the interaction between moment and tension at failure is essentially linear (geometrically non-linear analysis). For those cases governed by ply-failure, the Tsai-Hill criterion provides a good overall representation. It is noted that even though it might be possible to obtain a closer "fit" of

Type	Maximum strain	Tsai-Hill*	Energy**
I	Y	Y	Y, Γ_1
II	Y	Y	Y, Γ_1
III		Y	Y, Γ_2
IV			Y, Γ_3

(* all for same material parameters,
** different material parameters Γ_1, Γ_2, Γ_3)

Table 6.1:

the computations to individual sets of data for the separate lay-ups, the author has refrained from doing so in the interest of applying as uniform a criterion as possible to all tests and configurations.

It is found that all failures can be described in terms of a common fracture principle; the stress or strain criteria are interchangeable with the fracture energy computations, provided one allows for different values of associated fracture energies as shown in table 6.1. "Y" denotes a failure criterion which can be used for the specimen type.

The effect of temperature on the failure manifests itself primarily in a lowering of the load levels, leaving the modes of failure essentially unaltered. While at temperatures within a few degrees of the glass transition, this behavior may change, particularly as the result of more pronounced time dependent material response, in the present environment the temperature primarily reduces the material strength. To describe a consistent failure behavior, one must incorporate the thermally induced stresses in the overall evaluation, since the latter contribute a significant portion of the total and final stresses in the compound lay-up.

The specimens inviting the fracture mode of failure (Type IV specimens) provide the highest strength as measured by load carrying ability; it is nearly twice "as strong" as the other types of specimens which failed by ply fracture. However, the "stronger" configuration allowed for a markedly smaller margin of safety after failure

initiation than the ply-failure modes; the latter provided a margin of about 30 to 45% beyond the load at failure initiation. Thus, the preference of one over the other lay-up in applications is not completely clear: While the higher load carrying ability is desirable, the margin of error allowed in designs of engineering structures is also smaller. On the other hand, if both analysis tools and manufacturing process can allow for a sufficiently accurate failure estimation, the Type IV configuration may be the preferred choice in structural applications.

Bibliography

[1] Daniel, I. M. and Ishai, O. (1994), *Engineering Mechanics of Composite Materials*, Oxford University Press, Inc.

[2] Tan, S. C. (1994), *Stress Concentrations in Laminated Composites*, Technomic Publishing Co., Inc.

[3] Wilhite, A. W. and Shaw, R. J. (1997), "HSCT research picks up speed," Aerospace America, August, pp. 24-41.

[4] Lin, K. Y. and Hartman, H. H. (1989), "Numerical Analysis of Stress Singularities at a Bonded Anisotropic Wedge," Engineering Fracture Mechanics,32(2), pp. 211-224.

[5] Zenkert, D., Schubert, O. and Burman, M. (1997), "Fracture Initiation in Foam-Core Sandwich Structures Due to Singular Stresses at Corners of Flawed Butt Joints," Mechanics of Composite Materials and Structures, 4, pp. 1-21.

[6] Kassapoglou, C. and DiNicola, A. J. (1992), "Efficient Stress Solutions at Skin Stiffener Interfaces of Composite Stiffened Panels," AIAA Journal, 30(7), pp. 1833-1839.

[7] Bhat, N. V. and Lagace, P. A. (1994), "An Analytical Method for the Evaluation of Interlaminar Stresses Due to Material Discontinuities," Journal of Composite Materials, 28(3), pp. 190-210.

[8] Botting, A. D., Vizzini, A. J. and Lee, S. W. (1996), "Effect of Ply-Drop Configuration on Delamination Strength of Tapered Composite Structures," AIAA Journal, 34(8), pp. 1650-1656.

[9] Hyer, M.W., Loup, D. C. and Starnes Jr., J. H. (1990), "Stiffener/Skin Interactions in Pressure-Loaded Composite Panels," AIAA Journal, 28(3), pp. 532-537.

[10] Kubr, T. J. (1990), "Stresses Near a Change of Thickness in a Continuous- Fiber-Composite Plate," Ae.E. Thesis, Graduate Aeronautical Laboratories, California Institute of Technology, Pasadena, CA.

[11] Gortsema, S. C. (1992), "An Experimental Investigation of the Failure of a Stepped Composite Plate," Ae.E. Thesis, Graduate Aeronautical Laboratories, California Institute of Technology, Pasadena, CA.

[12] Martin, R. H. (1996), "Local Fracture Mechanics Analysis of Stringer Pull-off and Delamination in a Post-Buckled Compression Panel," Applied Composite Materials, 3, pp. 249-264.

[13] Vinson, J. R. and Sierakowski, R. L. (1986), *The Behavior of Structures Composed of Composite Materials*, Martinus Nijhoff Publishers, Dordrecht, The Netherlands.

[14] Hibbitt, Karlsson and Sorensen, Inc. (1995), *ABAQUS Theory Manual, Version 5.5.* Hibbitt, Karlsson and Sorensen, Inc.

[15] Pipes, R. B. and Pagano, N. J. (1970), "Interlaminar Stresses in Composite Laminates under Axial Extension," Journal of Composite Materials, 4, pp. 538-548.

[16] Whitney, J. M. and Nuismer, R.J. (1974), "Stress Fracture Criteria for Laminated Composites Containing Stress Concentrations," Journal of Composite Materials, 8, pp. 253-265.

[17] Ribicki, E. F., Schmueser, D. W. and Fox, J. (1977), "An Energy Release Rate Approach For Stable Crack Growth in the Free-Edge Delamination Problem," Journal of Composite Materials, 11, pp. 470-487.

[18] Whitney, J. M., Browning, C. E. and Hoogsteden, W. (1982), "A Double Cantilever Beam Test for Characterizing Mode I Delamination of Composite Materials," Journal of Reinforced Plastics and Composites, 1, pp. 297-313.

[19] Williams, M. L. (1957), "On the stress distribution at the Base of a Stationary Crack," Journal of Applied Mechanics, 24, pp. 109-114.

[20] McNally, D. J. (1985), "Inspection of Composite Rocket Motor Cases Using Acoustic Emission," Materials Evaluation, 43, pp. 728-739.

[21] Waters, A. (1996), Private Communication, Lockheed-Georgia date of 2-8-1982.

[22] U.S. Army Research Laboratory, *Composite Materials Handbook, MIL-HDBK-17.* (Refer webpage www.ccm.udel.edu/army/.)

[23] Liu, C., Huang, Y., Lovato, M. L., and Stout, M. G. (1996), "Measurement of the Fracture Toughness of a Fiber-Reinforced Composite Using the Brazilian Disk Sample Geometry," Submitted to the Int. J. of Fracture.

.1 Laminate Stiffnesses

The matrices A_{ij}, B_{ij}, and D_{ij} in laminate consitutive relation are listed for each type. The matrix A is the same for all types.

Type I - Plate

$$[A] = \begin{bmatrix} 714924. & 218819. & 0.5 \\ 218819. & 714889. & 17.1 \\ 0.5 & 17.1 & 248043. \end{bmatrix}, [B] = \begin{bmatrix} 12. & -1.5 & -1.3 \\ -1.5 & -49. & 3.9 \\ -1.3 & 3.9 & 0. \end{bmatrix} \times 10^{-5}$$

$$[D] = \begin{bmatrix} 227.3 & 81.0 & 56.9 \\ 81.0 & 606.7 & 56.9 \\ 56.9 & 56.9 & 96.6 \end{bmatrix}$$

Type I - Plate and Stiffener

$$[A] = \begin{bmatrix} 1429850. & 437639. & 1.0 \\ 437639. & 1429850. & 34.2 \\ 1.0 & 34.2 & 496087. \end{bmatrix}, [B] = \begin{bmatrix} -48.8 & -36.0 & 12.2 \\ -36.0 & -106.2 & 9.8 \\ 12.2 & 9.8 & -37.8 \end{bmatrix} \times 10^{-4}$$

$$[D] = \begin{bmatrix} 3121.7 & 862.3 & 2.5 \times 10^{-3} \\ 862.3 & 3121.6 & 8.0 \times 10^{-2} \\ 2.5 \times 10^{-3} & 8.0 \times 10^{-2} & 987.0 \end{bmatrix}$$

Type II - Plate

$$[B] = \begin{bmatrix} -2.4 & -1.2 & 0. \\ -1.2 & -4.9 & 0. \\ 0. & 0. & 0. \end{bmatrix} \times 10^{-4}$$

$$[D] = \begin{bmatrix} 231.8 & 152.4 & -94.8 \\ 152.4 & 459.4 & -94.8 \\ -94.8 & -94.8 & 168.0 \end{bmatrix}$$

Type II - Plate and Stiffener

$$[B] = \begin{bmatrix} -78.1 & -19.5 & 9.8 \\ -19.5 & -107.4 & 4.9 \\ 9.8 & 4.9 & -19.5 \end{bmatrix} \times 10^{-4}$$

$$[D] = \begin{bmatrix} 2751.3 & 1005.0 & 2.3 \times 10^{-3} \\ 1005.0 & 3206.4 & 7.6 \times 10^{-2} \\ 2.3 \times 10^{-3} & 7.6 \times 10^{-2} & 1129.7 \end{bmatrix}$$

Type III - Plate

$$[B] = \begin{bmatrix} 12. & -1.5 & -1.3 \\ -1.5 & -49. & 3.9 \\ -1.3 & 3.9 & 0. \end{bmatrix} \times 10^{-5}$$

$$[D] = \begin{bmatrix} 227.3 & 81.0 & -56.9 \\ 81.0 & 606.7 & -56.9 \\ -56.9 & -56.9 & 96.6 \end{bmatrix}$$

Type III - Plate and Stiffener

$$[B] = \begin{bmatrix} -62.3 & -35.7 & -9.2 \\ -35.7 & -87.9 & -8.7 \\ -9.2 & -8.7 & -37.2 \end{bmatrix} \times 10^{-4}$$

$$[D] = \begin{bmatrix} 2742.3 & 862.3 & 2.9 \times 10^{-3} \\ 862.3 & 3501.0 & 9.7 \times 10^{-2} \\ 2.9 \times 10^{-3} & 9.7 \times 10^{-2} & 986.9 \end{bmatrix}$$

Type IV - Plate

$$[B] = \begin{bmatrix} 0. & -3.1 & 0. \\ -3.1 & 12.2 & 0. \\ 0. & 0. & 0. \end{bmatrix} \times 10^{-5}$$

$$[D] = \begin{bmatrix} 606.7 & 81.0 & -56.9 \\ 81.0 & 227.3 & -56.9 \\ -56.9 & -56.9 & 96.6 \end{bmatrix}$$

Type IV - Plate and Stiffener

$$[B] = \begin{bmatrix} -68.4 & -36.0 & -9.8 \\ -36.0 & -86.7 & -9.8 \\ -9.8 & -9.8 & -37.8 \end{bmatrix} \times 10^{-4}$$

$$[D] = \begin{bmatrix} 3501.1 & 862.3 & 1.9 \times 10^{-3} \\ 862.3 & 2742.2 & 6.3 \times 10^{-2} \\ 1.9 \times 10^{-3} & 6.3 \times 10^{-2} & 986.9 \end{bmatrix}$$

.2 ABAQUS Input Program

.2.1 Main Program for Combined Loading - Type I

```
*Heading
Combined Loading - Type 1 - e=0.1, T=126 lbs
*PREPRINT, ECHO=NO, model=no
**
**Include node & element data
**
*INCLUDE, INPUT=e0.1.inp
*INCLUDE, INPUT=global-com2.inp
**
**====================
**MATERIAL DEFINITION
** (For other types, change orientations of each ELSET.)
**====================
*SOLID SECTION, MATERIAL=LAYER, ELSET=P1, ORIENTATION=L90
*SOLID SECTION, MATERIAL=LAYER, ELSET=P2, ORIENTATION=L45
*SOLID SECTION, MATERIAL=LAYER, ELSET=P3, ORIENTATION=L0
*SOLID SECTION, MATERIAL=LAYER, ELSET=P4, ORIENTATION=L-45
*SOLID SECTION, MATERIAL=LAYER, ELSET=P5, ORIENTATION=L-45
*SOLID SECTION, MATERIAL=LAYER, ELSET=P6, ORIENTATION=L0
*SOLID SECTION, MATERIAL=LAYER, ELSET=P7, ORIENTATION=L45
*SOLID SECTION, MATERIAL=LAYER, ELSET=P8, ORIENTATION=L90
*SOLID SECTION, MATERIAL=LAYER, ELSET=S1, ORIENTATION=L0
*SOLID SECTION, MATERIAL=LAYER, ELSET=S2, ORIENTATION=L-45
*SOLID SECTION, MATERIAL=LAYER, ELSET=S3, ORIENTATION=L90
*SOLID SECTION, MATERIAL=LAYER, ELSET=S4, ORIENTATION=L45
*SOLID SECTION, MATERIAL=LAYER, ELSET=S5, ORIENTATION=L45
*SOLID SECTION, MATERIAL=LAYER, ELSET=S6, ORIENTATION=L90
*SOLID SECTION, MATERIAL=LAYER, ELSET=S7, ORIENTATION=L-45
*SOLID SECTION, MATERIAL=LAYER, ELSET=S8, ORIENTATION=L0
*MATERIAL, NAME=LAYER
*ELASTIC, TYPE=ENGINEERING CONSTANTS
20.5E6, 1.67E6, 1.67E6, 0.3, 0.3, 0.1, 8.7E5, 8.7E5
8.7E5
*ORIENTATION, NAME=L90
1.,0.,0., 0.,1.,0.
3,90.
*ORIENTATION, NAME=L0
1.,0.,0., 0.,1.,0.
3,0.
*ORIENTATION, NAME=L45
1.,0.,0., 0.,1.,0.
3,45.
*ORIENTATION, NAME=L-45
1.,0.,0., 0.,1.,0.
3,-45.
*MATERIAL, NAME=STEEL
*ELASTIC
29.0E6, 0.3
**=========
**LOADING
**=========
*ELSET, GENERATE, ELSET=SEC
13, 16
```

```
2013, 2016
4013, 4016
6013, 6016
8013, 8016
10013, 10016
12013, 12016
14013, 14016
*NSET, NSET=MASTER
40815, 50815
*NSET, GENERATE, NSET=EDLINE
21, 25
**
*STEP, NLGEOM, INC=70
*STATIC
0.01,1
*BOUNDARY
40815, 2, 4, 0.
40815, 6, 6, 0.
50815, 1, 4, 0.
50815, 6, 6, 0.
**
*CLOAD
40815, 1, -126.
**-----------------
** Output Request
**-----------------
*EL PRINT, ELSET=SEC, FREQUENCY=70
COORD, S11, S22, S33, S12, S13, S23
*NODE PRINT, NSET=DEFL, FREQUENCY=70
U
*NODE PRINT, NSET=EDLINE
U
*NODE PRINT, NSET=MASTER
RF
*NODE FILE, NSET=SUB, FREQUENCY=70
U, RF
*RESTART, WRITE, FREQUENCY=70
*END STEP
```

.2.2 Fixture for Combined Loading - Eccentricity = 0.1in

```
*HEADING
Fixtures for Combined-Load Tests, e=0.1[in]
*PREPRINT, ECHO=NO, model=no
**----------
** Left Tab
**----------
**
** Nodes on the specimen
**
*NODE
1, 0., 0., 0.
5, 0., 1., 0.
6, 0.75, 0., 0.
10, 0.75, 1., 0.
1005, 5.75, 0., 0.
1009, 5.75, 1., 0.
1010, 6.5, 0., 0.
1014, 6.5, 1., 0.
*NGEN
1, 5
6, 10
1005, 1009
1010, 1014
*NSET, GENERATE, NSET=TEMP1
1, 10
**
*NCOPY, OLD SET=TEMP1, SHIFT, CHANGE NUMBER= 16000
0., 0., 0.08

*NCOPY, OLD SET=TEMP1, SHIFT, CHANGE NUMBER= 40100
0., 0., 0.33

*NCOPY, OLD SET=TEMP1, SHIFT, CHANGE NUMBER= 40000
0., 0., -1.

*NCOPY, OLD SET=TEMP1, SHIFT, CHANGE NUMBER= 40200
0., 0., -1.5

**
*NSET, NSET= EDGE1
2, 3, 4
*NCOPY, OLD SET= EDGE1, SHIFT, CHANGE NUMBER= 40400, NEW SET=EDGE1A
-1.375, 0., -1.5

*NCOPY, OLD SET= EDGE1A, SHIFT, CHANGE NUMBER= 10, NEW SET=EDGE1B
1., 0., 0.

*NFILL, NSET=BOT
EDGE1A, EDGE1B, 2, 5
**
*NCOPY, OLD SET=BOT, SHIFT, CHANGE NUMBER= 100
0., 0., 0.5

**=========================================================
** Shift in Z direction = 1.04 + e
```

```
**
*NCOPY, OLD SET=BOT, SHIFT, CHANGE NUMBER= 200
0., 0., 1.14

**=============================================================
*NODE, NSET=LFACE1
40901, 0., -0.5, 0.33
40902, 0., -0.5, 0.08
40903, 0., -0.5, 0.
40904, 0., -0.5, -1.
40905, 0.75, -0.5, 0.33
40906, 0.75, -0.5, 0.08
40907, 0.75, -0.5, 0.
40908, 0.75, -0.5, -1.
*NCOPY, OLD SET= LFACE1, SHIFT, CHANGE NUMBER= 10
0., 0.4, 0.

*NCOPY, OLD SET= LFACE1, SHIFT, CHANGE NUMBER= 20
0., 1.6, 0.

*NCOPY, OLD SET= LFACE1, SHIFT, CHANGE NUMBER= 30
0., 2., 0.

**
**NODES on a CIRCLE
**=================================================
** For the following three nodes,
** Z-coordinate = 0.04 + e
**
*NODE
40801, -1.375, 0.25, 0.14
40815, -0.875, 0.25, 0.14
40805, -0.375, 0.25, 0.14
**---------------------------------
** For the following three nodes,
** Z-coordinate = 0.04 + e + 0.5
**
*NODE
40802, -1.375, 0.25, 0.64
40803, -0.875, 0.25, 0.64
40804, -0.375, 0.25, 0.64
**---------------------------------
** For the following two nodes,
** Z-coordinate = 0.04 + e - 0.25
**
*NODE
40806, -0.875, 0.25, -0.11
40814, -0.875, 0.25, -0.11
**=================================================
*NGEN, LINE=C
40806, 40814, 1, 40815, , , , 0., 1., 0.
*NSET, GENERATE, NSET=SIDEUP
40801, 40815
*NCOPY, OLD SET= SIDEUP, CHANGE NUMBER=20, SHIFT
0., 0.25, 0.

*NCOPY, OLD SET= SIDEUP, CHANGE NUMBER=40, SHIFT
0., 0.5, 0.
```

```
**-------------------------------------------------
** ELEMENT DEFINITION
**-------------------------------------------------
*ELEMENT, TYPE=C3D8I, ELSET=SUBEL1
40001, 40001, 40006, 40007, 40002, 1, 6, 7, 2
40101, 16001, 16006, 16007, 16002, 40101, 40106, 40107, 40102
40201, 40201, 40206, 40207, 40202, 40001, 40006, 40007, 40002
40402, 40402, 40407, 40408, 40403, 40502, 40507, 40508, 40503
40502, 40502, 40507, 40508, 40503, 40602, 40607, 40608, 40603
**
40410, 40412, 40202, 40203, 40413, 40512, 40002, 40003, 40513
40901, 40902, 40906, 40916, 40912, 40901, 40905, 40915, 40911
40921, 40922, 40926, 40936, 40932, 40921, 40925, 40935, 40931
**
40005, 40005, 40010, 40928, 40924, 5, 10, 40927, 40923
40105, 16005, 16010, 40926, 40922, 40105, 40110, 40925, 40921
40006, 40914, 40918, 40006, 40001, 40913, 40917, 6, 1
40106, 40912, 40916, 16006, 16001, 40911, 40915, 40106, 40101
**
40801, 40602, 40807, 40827, 40603, 40801, 40808, 40828, 40821
40802, 40801, 40808, 40828, 40821, 40802, 40809, 40829, 40822
40806, 40805, 40812, 40832, 40825, 40612, 40813, 40833, 40613
40807, 40612, 40813, 40833, 40613, 40607, 40806, 40826, 40608
40808, 40607, 40806, 40826, 40608, 40602, 40807, 40827, 40603
40821, 40603, 40827, 40847, 40604, 40821, 40828, 40848, 40841
40822, 40821, 40828, 40848, 40841, 40822, 40829, 40849, 40842
40826, 40825, 40832, 40852, 40845, 40613, 40833, 40853, 40614
40827, 40613, 40833, 40853, 40614, 40608, 40826, 40846, 40609
40828, 40608, 40826, 40846, 40609, 40603, 40827, 40847, 40604
*ELGEN, ELSET=SUBEL2
40001, 4, 1, 1
40101, 4, 1, 1
40201, 4, 1, 1
40402, 2, 1, 1, 2, 5, 5
40502, 2, 1, 1, 2, 5, 5
40410, 2, 1, 1
**
40901, 3, 1, 1
40921, 3, 1, 1
**
40802, 4, 1, 1
40822, 4, 1, 1
**
*ELEMENT, TYPE=R3D4
40811, 40806, 40807, 40827, 40826
40831, 40826, 40827, 40847, 40846
*Elgen, Elset=pin1
40811, 8
40831, 8
*RIGID BODY, ELSET= PIN1, REF NODE=40815
**---------------
** RIGHT TAB
**---------------
*NCOPY, OLD SET=TEMP1, SHIFT, CHANGE NUMBER= 17004
5.75, 0., 0.08

*NCOPY, OLD SET=TEMP1, SHIFT, CHANGE NUMBER= 50000
5.75, 0., -1.
```

```
*NCOPY, OLD SET=TEMP1, SHIFT, CHANGE NUMBER= 50200
5.75, 0., -1.5

*NCOPY, OLD SET=TEMP1, SHIFT, CHANGE NUMBER= 50100
5.75, 0., 0.33

**
*NCOPY, OLD SET=LFACE1, SHIFT, CHANGE NUMBER= 10000
5.75, 0., 0.

*NCOPY, OLD SET=LFACE1, SHIFT, CHANGE NUMBER= 10010
5.75, 0.4, 0.

*NCOPY, OLD SET=LFACE1, SHIFT, CHANGE NUMBER= 10020
5.75, 1.6, 0.

*NCOPY, OLD SET=LFACE1, SHIFT, CHANGE NUMBER= 10030
5.75, 2., 0.

**
*NCOPY, OLD SET=BOT, SHIFT, CHANGE NUMBER= 10000
8.25, 0., 0.

*NCOPY, OLD SET=BOT, SHIFT, CHANGE NUMBER= 10100
8.25, 0., 0.5

*NSET, NSET=BOT1
40602, 40603, 40604, 40607, 40608, 40609, 40612, 40613, 40614
*NCOPY, OLD SET=BOT1, SHIFT, CHANGE NUMBER= 10000
8.25, 0., 0.

**
*NSET, GENERATE, NSET=SIDEUP1
40801, 40815
40821, 40835
40841, 40855
*NCOPY, OLD SET= SIDEUP1, CHANGE NUMBER=10000, SHIFT
8.25, 0., 0.

**-----------------------------------------------------
** ELEMENT DEFINITION
**-----------------------------------------------------
*ELEMENT, TYPE=C3D8I, ELSET=SUBELA
50001, 50001, 50006, 50007, 50002, 1005, 1010, 1011, 1006
50101, 17005, 17010, 17011, 17006, 50101, 50106, 50107, 50102
50201, 50201, 50206, 50207, 50202, 50001, 50006, 50007, 50002
50402, 50402, 50407, 50408, 50403, 50502, 50507, 50508, 50503
50502, 50502, 50507, 50508, 50503, 50602, 50607, 50608, 50603
**
50410, 50207, 50402, 50403, 50208, 50007, 50502, 50503, 50008
50901, 50902, 50906, 50916, 50912, 50901, 50905, 50915, 50911
50921, 50922, 50926, 50936, 50932, 50921, 50925, 50935, 50931
**
50005, 50005, 50010, 50928, 50924, 1009, 1014, 50927, 50923
50105, 17009, 17014, 50926, 50922, 50105, 50110, 50925, 50921
50006, 50914, 50918, 50006, 50001, 50913, 50917, 1010, 1005
50106, 50912, 50916, 17010, 17005, 50911, 50915, 50106, 50101
**
```

```
50801, 50602, 50807, 50827, 50603, 50801, 50808, 50828, 50821
50802, 50801, 50808, 50828, 50821, 50802, 50809, 50829, 50822
50806, 50805, 50812, 50832, 50825, 50612, 50813, 50833, 50613
50807, 50612, 50813, 50833, 50613, 50607, 50806, 50826, 50608
50808, 50607, 50806, 50826, 50608, 50602, 50807, 50827, 50603
**
50821, 50603, 50827, 50847, 50604, 50821, 50828, 50848, 50841
50822, 50821, 50828, 50848, 50841, 50822, 50829, 50849, 50842
50826, 50825, 50832, 50852, 50845, 50613, 50833, 50853, 50614
50827, 50613, 50833, 50853, 50614, 50608, 50826, 50846, 50609
50828, 50608, 50826, 50846, 50609, 50603, 50827, 50847, 50604
*ELGEN, ELSET=SUBELB
50001, 4, 1, 1
50101, 4, 1, 1
50201, 4, 1, 1
50402, 2, 1, 1, 2, 5, 5
50502, 2, 1, 1, 2, 5, 5
50410, 2, 1, 1
**
50901, 3, 1, 1
50921, 3, 1, 1
**
50802, 4, 1, 1
50822, 4, 1, 1
**
*ELSET, ELSET=TAB
SUBEL1, SUBEL2, SUBELA, SUBELB
**
*ELEMENT, TYPE=R3D4
50811, 50806, 50807, 50827, 50826
50831, 50826, 50827, 50847, 50846
*ELGEN, ELSET=PIN2
50811, 8
50831, 8
*RIGID BODY, ELSET= PIN2, REF NODE=50815
```

.2.3 global-com2.inp

```
*HEADING
Global Model of a Specimen for Combined Loading
**=========================================
**
** Node Generation
**
**=========================================
*NSET, GENERATE, NSET=L1
1, 5
*NSET, GENERATE, NSET=L1a
6, 10
**
*NCOPY, OLD SET= L1, CHANGE NUMBER=20, SHIFT, NEW SET=L2
1.75, 0., 0.

*NCOPY, OLD SET= L1, CHANGE NUMBER=35, SHIFT, NEW SET=L3
3.25, 0., 0.

*NCOPY, OLD SET= L1, CHANGE NUMBER=50, SHIFT, NEW SET=L4
4.75, 0., 0.

*NCOPY, OLD SET= L1, CHANGE NUMBER=65, SHIFT, NEW SET=L5
5.75, 0., 0.

*NFILL
L1a, L2, 3, 5
L2, L3, 3, 5
L4, L5, 3, 5
L3, L4, 3, 5
**
*NSET, GENERATE, NSET=BOTSFC
1, 65
1005, 1014
*NCOPY, CHANGE NUMBER= 16000, OLD SET= BOTSFC, SHIFT, NEW SET=TOPSFC
0., 0., 0.08

*NFILL
BOTSFC, TOPSFC, 8, 2000
*NSET, GENERATE, NSET=STIFF
16021, 16055
*NCOPY, CHANGE NUMBER= 16000, OLD SET= STIFF, SHIFT, NEW SET=STIFF1
0., 0., 0.08

*NFILL
STIFF, STIFF1, 8, 2000
**---------------------------
** Node Sets for Output
**---------------------------
*NSET, GENERATE, NSET=DEFL
1, 61, 5
1005, 1010, 5
*NSET, NSET=SUB, GENERATE
1, 40
2001, 2040
4001, 4040
6001, 6040
8001, 8040
```

```
10001, 10040
12001, 12040
14001, 14040
16001, 16040
18021, 18040
20021, 20040
22021, 22040
24021, 24040
26021, 26040
28021, 28040
30021, 30040
32021, 32040
**=========================================
**
** Element Generation
**
**=========================================
*ELEMENT, TYPE=C3D8I
1, 1, 6, 7, 2, 2001, 2006, 2007, 2002
61, 61, 1005, 1006, 62, 2061, 3005, 3006, 2062
1005, 1005, 1010, 1011, 1006, 3005, 3010, 3011, 3006
*ELGEN, ELSET=P1
1, 4, 1, 1, 12, 5, 4
61, 4, 1, 1
1005, 4, 1, 1
*ELCOPY,ELEMENT SHIFT=2000, OLD SET=P1, SHIFT NODES=2000, NEWSET=P2
*ELCOPY,ELEMENT SHIFT=2000, OLD SET=P2, SHIFT NODES=2000, NEWSET=P3
*ELCOPY,ELEMENT SHIFT=2000, OLD SET=P3, SHIFT NODES=2000, NEWSET=P4
*ELCOPY,ELEMENT SHIFT=2000, OLD SET=P4, SHIFT NODES=2000, NEWSET=P5
*ELCOPY,ELEMENT SHIFT=2000, OLD SET=P5, SHIFT NODES=2000, NEWSET=P6
*ELCOPY,ELEMENT SHIFT=2000, OLD SET=P6, SHIFT NODES=2000, NEWSET=P7
*ELCOPY,ELEMENT SHIFT=2000, OLD SET=P7, SHIFT NODES=2000, NEWSET=P8
*ELSET, ELSET=S11, GENERATE
14017, 14040
*ELCOPY,ELEMENT SHIFT=2000, OLD SET=S11, SHIFT NODES=2000, NEWSET=S1
*ELCOPY,ELEMENT SHIFT=2000, OLD SET=S1, SHIFT NODES=2000, NEWSET=S2
*ELCOPY,ELEMENT SHIFT=2000, OLD SET=S2, SHIFT NODES=2000, NEWSET=S3
*ELCOPY,ELEMENT SHIFT=2000, OLD SET=S3, SHIFT NODES=2000, NEWSET=S4
*ELCOPY,ELEMENT SHIFT=2000, OLD SET=S4, SHIFT NODES=2000, NEWSET=S5
*ELCOPY,ELEMENT SHIFT=2000, OLD SET=S5, SHIFT NODES=2000, NEWSET=S6
*ELCOPY,ELEMENT SHIFT=2000, OLD SET=S6, SHIFT NODES=2000, NEWSET=S7
*ELCOPY,ELEMENT SHIFT=2000, OLD SET=S7, SHIFT NODES=2000, NEWSET=S8
```

.2.4 Submodel for Type I

```
*HEADING
SUB MODEL
*PREPRINT, ECHO=NO, MODEL=NO
*Node
1, 1.251, 0., 0.
2001, 1.251, 0.5, 0.
4001, 1.251, 1., 0.
80001, 1.251, 0., 0.08
82001, 1.251, 0.5, 0.08
84001, 1.251, 1., 0.08
*NGEN, NSET=H1
1,80001, 10000
*NGEN, NSET=H2
2001, 82001, 10000
*NGEN, NSET=H3
4001, 84001, 10000
*NFILL, BIAS=0.8, NSET=F1
H1,H2, 5, 400
*NFILL, BIAS=1.25, NSET=F2
H2,H3, 5, 400
*NSET,NSET=FACE1
F1, F2
**========================
**NODE GENERATION - PLATE
**========================
*NCOPY,CHANGE NUMBER= 5 ,OLD SET=FACE1,SHIFT,NEW SET=FACE2
0.499, 0., 0.
*NFILL,BIAS=1.25
FACE1,FACE2, 5
*NCOPY,CHANGE NUMBER= 10,OLD SET=FACE1,SHIFT,NEW SET=FACE3
0.998, 0., 0.
*NFILL,BIAS=0.8
FACE2,FACE3, 5
**============================
**NODE GENERATION - STIFFNER
**============================
*NSET,NSET=LINE3,GENERATE
80006,84006, 400
*NSET,NSET=LINE6,GENERATE
80011,84011, 400
*NCOPY,CHANGE NUMBER= 10000,OLD SET=LINE3,SHIFT,NEW SET=LINE4
0., 0., 0.01
*NCOPY,CHANGE NUMBER= 80000,OLD SET=LINE3,SHIFT,NEW SET=LINE5
0., 0., 0.08
*NCOPY,CHANGE NUMBER= 10000,OLD SET=LINE6,SHIFT,NEW SET=LINE7
0., 0., 0.01
*NCOPY,CHANGE NUMBER= 80000,OLD SET=LINE6,SHIFT,NEW SET=LINE8
0., 0., 0.08
*NFILL, NSET=FACE10
LINE4,LINE5, 7, 10000
*NFILL, NSET=FACE11
LINE7,LINE8, 7, 10000
*NFILL, BIAS=0.8
FACE10,FACE11, 5
*NSET,NSET=FROM
FACE1, FACE3, FACE11
```

```
**====================
**ELEMENT GENERATION
**====================
*ELEMENT,TYPE=C3D8I
1,1,2,402,401,10001,10002,10402,10401
*ELEMENT,TYPE=C3D8I
80006, 80006, 80007, 80407, 80406, 90006, 90007, 90407, 90406
*ELGEN, ELSET=P1
1, 10, 400, 400, 10, 1, 1
*ELCOPY,ELEMENT SHIFT=10000, OLD SET=P1, SHIFT NODES=10000, NEWSET=P2
*ELCOPY,ELEMENT SHIFT=10000, OLD SET=P2, SHIFT NODES=10000, NEWSET=P3
*ELCOPY,ELEMENT SHIFT=10000, OLD SET=P3, SHIFT NODES=10000, NEWSET=P4
*ELCOPY,ELEMENT SHIFT=10000, OLD SET=P4, SHIFT NODES=10000, NEWSET=P5
*ELCOPY,ELEMENT SHIFT=10000, OLD SET=P5, SHIFT NODES=10000, NEWSET=P6
*ELCOPY,ELEMENT SHIFT=10000, OLD SET=P6, SHIFT NODES=10000, NEWSET=P7
*ELCOPY,ELEMENT SHIFT=10000, OLD SET=P7, SHIFT NODES=10000, NEWSET=P8
*ELGEN,ELSET=S1
80006, 10, 400, 400, 5, 1, 1
*ELCOPY,ELEMENT SHIFT=10000, OLD SET=S1, SHIFT NODES=10000, NEWSET=S2
*ELCOPY,ELEMENT SHIFT=10000, OLD SET=S2, SHIFT NODES=10000, NEWSET=S3
*ELCOPY,ELEMENT SHIFT=10000, OLD SET=S3, SHIFT NODES=10000, NEWSET=S4
*ELCOPY,ELEMENT SHIFT=10000, OLD SET=S4, SHIFT NODES=10000, NEWSET=S5
*ELCOPY,ELEMENT SHIFT=10000, OLD SET=S5, SHIFT NODES=10000, NEWSET=S6
*ELCOPY,ELEMENT SHIFT=10000, OLD SET=S6, SHIFT NODES=10000, NEWSET=S7
*ELCOPY,ELEMENT SHIFT=10000, OLD SET=S7, SHIFT NODES=10000, NEWSET=S8
*ELSET, ELSET=SEC1,GENERATE
5, 3605, 400
10005, 13605, 400
20005, 23605, 400
30005, 33605, 400
40005, 43605, 400
50005, 53605, 400
60005, 63605, 400
70005, 73605, 400
*ELSET, ELSET=TOP1,GENERATE
70002, 73602, 400
70003, 73603, 400
70004, 73604, 400
70005, 73605, 400
70006, 73606, 400
70007, 73607, 400
**====================
**MATERIAL DEFINITION
**====================
*SOLID SECTION, MATERIAL=LAYER, ELSET=P1, ORIENTATION=L90
*SOLID SECTION, MATERIAL=LAYER, ELSET=P2, ORIENTATION=L45
*SOLID SECTION, MATERIAL=LAYER, ELSET=P3, ORIENTATION=L0
*SOLID SECTION, MATERIAL=LAYER, ELSET=P4, ORIENTATION=L-45
*SOLID SECTION, MATERIAL=LAYER, ELSET=P5, ORIENTATION=L-45
*SOLID SECTION, MATERIAL=LAYER, ELSET=P6, ORIENTATION=L0
*SOLID SECTION, MATERIAL=LAYER, ELSET=P7, ORIENTATION=L45
*SOLID SECTION, MATERIAL=LAYER, ELSET=P8, ORIENTATION=L90
*SOLID SECTION, MATERIAL=LAYER, ELSET=S1, ORIENTATION=L0
*SOLID SECTION, MATERIAL=LAYER, ELSET=S2, ORIENTATION=L-45
*SOLID SECTION, MATERIAL=LAYER, ELSET=S3, ORIENTATION=L90
*SOLID SECTION, MATERIAL=LAYER, ELSET=S4, ORIENTATION=L45
*SOLID SECTION, MATERIAL=LAYER, ELSET=S5, ORIENTATION=L45
*SOLID SECTION, MATERIAL=LAYER, ELSET=S6, ORIENTATION=L90
*SOLID SECTION, MATERIAL=LAYER, ELSET=S7, ORIENTATION=L-45
```

```
*SOLID SECTION, MATERIAL=LAYER, ELSET=S8, ORIENTATION=LO
*MATERIAL, NAME=LAYER
*ELASTIC, TYPE=ENGINEERING CONSTANTS
20.5E6, 1.67E6, 1.67E6, 0.3, 0.3, 0.1, 8.7E5, 8.7E5
8.7E5
*ORIENTATION, NAME=L90
1.,0.,0., 0.,1.,0.
3,90.
*ORIENTATION, NAME=LO
1.,0.,0., 0.,1.,0.
3,0.
*ORIENTATION, NAME=L45
1.,0.,0., 0.,1.,0.
3,45.
*ORIENTATION, NAME=L-45
1.,0.,0., 0.,1.,0.
3,-45.
*SUBMODEL
FROM
**=========
**LOADING
**=========
*STEP, NLGEOM, INC=30
*STATIC
0.05, 1.
*BOUNDARY,SUBMODEL, step=2
from,1,3
*EL PRINT, ELSET=sec1, FREQUENCY = 30
coord,s11,s22,s33,s12,s13,s23
*EL PRINT, ELSET=TOP1, FREQUENCY = 30
coord,s11,s22,s33,s12,s13,s23
*EL PRINT, ELSET=TOP1, FREQUENCY = 30
coord,e11,e22,e33,e12,e13,e23
*RESTART, WRITE, FREQUENCY = 30
*END STEP
```